

# Flares in Open Clusters with K2.

## II. Pleiades, Hyades, Praesepe, Ruprecht 147, and M67

Ekaterina Ilin<sup>1</sup>, Sarah J. Schmidt<sup>1</sup>, Katja Poppenhäger<sup>1</sup>, James R. A. Davenport<sup>2</sup> and Klaus G. Strassmeier<sup>1</sup>

<sup>1</sup> Leibniz Institut für Astrophysik Potsdam

e-mail: eilin@aip.de

<sup>2</sup> University of Washington e-mail: jrad@uw.edu

Received XXX; accepted XXX

### ABSTRACT

**Context.** Flares can help us trace magnetic activity because they are bright and high-contrast on low mass stars.

**Aims.** This study aims to quantify flaring activity on these stars as a function of mass and age.

**Methods.** We searched the light curves of open cluster stars in K2 time-domain photometry for flares using the open-source software packages K2SC and AltaiPony. K2SC was used to remove instrumental and astrophysical variability from K2 light curves, and AltaiPony to search and characterize the flare candidates. With the full K2 archive we added stars with a larger variety of ages and spectral types to the analysis of the previous study (Ilin et al. 2019) and manually confirmed a total of 2918 flares. We compared previous results from Praesepe to the flare frequency distributions (FFDs) in the Hyades, respectively. Ruprecht 147 filled in the age gap at 2.5 Gyr between the aforementioned young clusters and the 3.6 Gyr old M67.

**Results.** We find that the flare production mechanism is similar for the entire parameter space, following a power law relation with exponent  $\alpha \approx 1.9$ , but the flaring frequencies depend on both mass, and age. We discuss X and Y.

**Key words.** Methods: data analysis, Stars: activity, Stars: flare, Stars: low-mass

Use \titlerunning to supply a shorter title and/or \authorrunning to supply a shorter list of authors.

### 1. Introduction

Flares are explosions on stellar surfaces with a complex spatio-temporal and energetic phenomenology. We know that flares are magnetic re-connection events that lead to a change in field line topology and subsequent energy release (Priest & Forbes 2002). We can observe flares in nearly all electromagnetic bands, from radio to X-rays, and on all stars that possess a convection zone, from late F type stars to ultracool dwarfs (Gizis 2013). But even with continuous monitoring at high temporal resolution, the random occurrence of solar flares makes them costly observing targets, especially in coordinated multi-band observations. In integrated light, most solar flares have a far too low contrast and intensity to be observable. Stellar flares on cool stars have two advantages in this respect. They are often bright, enhancing stellar flux by up to several orders of magnitude, and they typically exhibit blackbody emission at temperatures significantly higher than their stars' photospheres.

With the evidence that the physical processes that cause flares on the Sun and other stars are the same (Karoff 2016), solar and stellar flares can inform each other (Shibayama et al. 2013). Inconsistencies in extrapolations from solar to stellar conditions (Aarnio et al. 2011; Aarnio et al. 2012; Drake et al. 2013) provide valuable clues to the differences in magnetic properties between Sun and M dwarfs, too (Alvarado-Gómez et al. 2018). Large surveys like Kepler and TESS enable statistical flare studies of stars that were not pre-selected for their activity (Walkowicz et al. 2011). Statistical studies of stellar flaring activity can help us understand the underlying physical processes CITE stellar surface magnetic fields, starspots (Davenport 2015; Howard

et al. 2019b), how flares relate to stellar angular momentum evolution (Mondrik et al. 2019; Howard et al. 2019b), how they affect the atmospheres of exoplanets (Lecavelier des Etangs et al. 2012; Loyd et al. 2018; Tilley et al. 2019; Howard et al. 2019a), and inform galactic archaeology (Howard et al. 2019a).

Basic parameters that affect flaring behaviour on stars are their masses, and ages. Ages can be controlled for in coeval groups of stars, and flaring-age studies in binaries showed consistency in activity for both components in the majority of targets (Lurie et al. 2015; Clarke et al. 2018). Open clusters present other coeval groups of stars with well-determined ages. Ilin et al. (2019) (hereafter PaperI) investigated the flaring activity of late-K to mid-M dwarfs in three open clusters (OCs), the Pleiades, Praesepe, and M67, using K2 time domain photometry. They analysed the flare frequency distributions (FFDs), with respect to different masses and cluster ages. For the cluster members, the light curves revealed that their flaring activity declines both with age and mass. The decline is faster for higher mass stars. Recently, Davenport et al. (2019) put forward an empirical parametrization of this flaring-mass-age relation based on FFDs. Flaring activity decays with age. Flaring fraction was observed to decline with galactic latitude for M dwarfs (Hilton et al. 2010)Howard+2019. Short rotation periods and high magnetic activity measured in H $\alpha$  are strongly correlated (West et al. 2015). According to gyrochronology, fast rotation indicates young age (Barnes 2003), and slows down as the star ages.

The present study aims to extend the results in PaperI to the age of Ruprecht 147 (2.5 Gyr) and M67 (3.6 Gyr), and both higher and lower masses than in the previous study. Because the Kepler satellite retired in fall 2018, we could use the complete K2

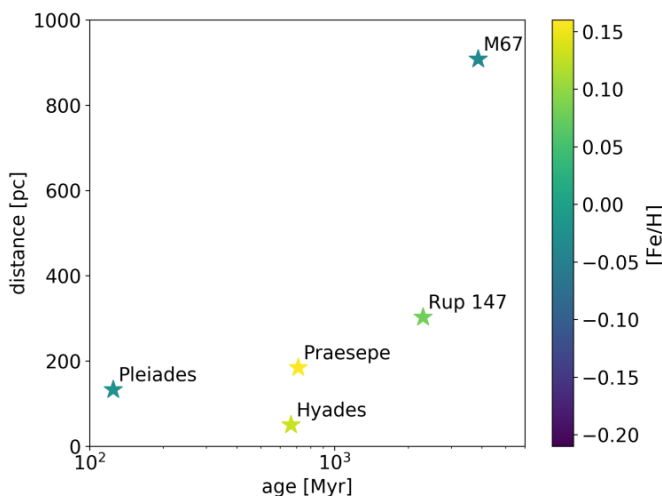


**Fig. 1.** The values for age, metallicity, and distance are approximate values from a compilation of existing literature, see Appendix B.

data set, and supplement all three OCs in PaperI with improved versions of already analysed light curves in campaigns 4 and 5, and with additional light curves from later campaigns. We discuss our results with respect to potential breaks in the power law distribution at high energies. Finally, we use the results to test the parametrization in Davenport et al. (2019).

## 2. Data

This work is based on K2 30-minute cadence light curves that were provided by the Kepler archives hosted at MAST. To assign  $T_{\text{eff}}$  to the stars for which these observation had been obtained we used multiband photometry from several all-sky surveys. To assign ages to the targeted stars, OC membership information was compiled from the literature. An overview over the cluster sample is presented in Table 1 and illustrated in Figure 1.

### 2.1. K2 light curves

The Kepler (Koch et al. 2010) spacecraft finished its follow-up mission K2 (Howell et al. 2014) in September 2018, after having completed nearly 20 80-day observing campaigns. Although Kepler and K2 data were already used in more than 2 400 publications in 2018, the public archive was still considered understudied (Barentsen et al. 2018). In this spirit we took up the analysis of a total of 2256 light curves where each light curve contained up to 80 uninterrupted days of 30 min cadence observations in white light ( $4, 200 - 9,000 \text{ \AA}$ ).

As K2 was conducted on the two-wheeled Kepler satellite, it was subjected to substantial drift motion (spacecraft roll, Van Cleve et al. 2016) and had an overall reduced pointing accuracy. To mitigate these effects, various solutions were developed (Vanderburg & Johnson 2014; Aigrain et al. 2016; ?; Luger et al. 2018). We used a minimally modified version of the K2 Systematics Correction pipeline (Aigrain et al. 2016), and used it to de-trend the 36th data release of the K2 data products. It was considered the final data release, and included a uniform, global reprocessing of most K2 campaigns using an improved data reduction pipeline<sup>1</sup>.

<sup>1</sup> <https://keplerscience.arc.nasa.gov/k2-uniform-global-reprocessing-underway.html>

## 2.2. Open clusters

We obtained membership information from multiple catalogs for each cluster. We cross-matched these catalogs on RA and declination within 3 arcsec. The resulting target lists were used to search the K2 archive. One part of the membership catalogs provided membership probabilities (Douglas et al. 2014; Cantat-Gaudin et al. 2018; Olivares et al. 2018; Reino et al. 2018; Gao 2018; Olivares et al. 2019). For the other part no probability was quoted (Rebull et al. 2016a; Douglas et al. 2017; Gaia Collaboration et al. 2018a), or qualitative classifiers were given (Curtis et al. 2013; Gonzalez 2016; Rebull et al. 2017). In the latter cases we assigned approximate probabilities anchored to the set threshold for inclusion into our final sample. Absence in a catalog did not decrease the likelihood of membership, as each catalog shows different selection biases which we did not address in this study. We set the threshold mean membership probability  $p$  for a target in our sample to 0.8.

We studied flaring activity in the low mass stars in five open clusters spanning from ZAMS to solar age. Table 1 provides an overview over the final sample. The literature overview of age, distance, and metallicity determinations is given in Table B.1 in the Appendix. Membership probability histograms of the final sample are displayed in Figure ??.

### 2.2.1. Pleiades

The Pleiades, a nearby ZAMS cluster, were observed in Campaign 4, and were treated in PaperI. We include the cluster in this work for completeness and to include improvements to (PaperI). We revisited the memberships from Rebull et al. (2016a), which were your in the previous work, and merged them with lists of members determined by Olivares et al. (2018); Gaia Collaboration et al. (2018a); and Cantat-Gaudin et al. (2018).

### 2.2.2. Hyades

The Hyades are a 0.6 Gyr old OC that were observed during Campaigns 4 and 13 with K2. It is about as old as Praesepe. We merged membership tables obtained from Douglas et al. (2014); Reino et al. (2018); and Gaia Collaboration et al. (2018a).

### 2.2.3. Praesepe

Praesepe appeared in Campaign 5, and was also treated in PaperI. It was then observed again during Campaigns 16, and 18. We revisited the memberships obtained by Douglas et al. (2014), and matched them to the members identified in Douglas et al. (2017); Rebull et al. (2017); Cantat-Gaudin et al. (2018); and Gaia Collaboration et al. (2018a).

### 2.2.4. Ruprecht 147

Ruprecht 147 is a 2.5 Gyr old OC observed during Campaign 7 with K2. We used the mean membership probabilities obtained from a number of studies (Curtis et al. 2013; Cantat-Gaudin et al. 2018; Olivares et al. 2019) combined with the members found by Gaia Collaboration et al. (2018a) to identify the most likely members.

**Table 1.** Open clusters.

	d [pc]	stars	LCs	flares	campaigns	age [Myr]	[Fe/H]
Pleiades	135.6	761	761	1606	1	135 ( <sup>25</sup> / <sub>25</sub> )	-0.04(0.03)
Hyades	46.0	171	171	396	2	690 ( <sup>100</sup> / <sub>160</sub> )	0.13(0.02)
Praesepe	185.5	964	964	906	3	750 ( <sup>7</sup> / <sub>3</sub> )	0.16(0.00)
Rup 147	305.0	53	53	9	1	2650 ( <sup>380</sup> / <sub>380</sub> )	0.08(0.07)
M67	908.0	307	307	1	3	3639 ( <sup>17</sup> / <sub>17</sub> )	-0.10(0.08)

**Notes.** The values for age, [Fe/H], and distance  $d$  are approximate values arrived at by a comparison of existing literature, which is detailed in Appendix B.1. The uncertainties are noted in parentheses. "stars" denotes the approximate number of cluster members with membership probability  $p > 0.8$ . "LCs" and "campaigns" is the number of available light curves and the K2 campaigns during which they were observed, respectively. "flares" is the number of confirmed flares found in each cluster.

### 2.2.5. M67

M67 is a solar-age, solar metallicity OC about 900 pc away. Multiple members were observed during Campaign 5, and revisited in Campaigns 16 and 18. We did not find any flares in M67 in Campaign 5 (PaperI) light curves of members identified by Gonzalez (2016). Campaigns 16 and 18 delivered both additional observations, and new targets to the sample. We merged the members from Gonzalez (2016) with a recent study based of Gaia DR2 data (Gao 2018).

## 2.3. Effective temperatures, stellar radii, and luminosities

### 2.3.1. Photometry and extinction correction

We determined effective temperatures  $T_{\text{eff}}$  using broadband photometry the Two Micron All Sky Survey (2MASS; Skrutskie et al. 2006), the Panoramic Survey Telescope and Rapid Response System (Pan-STARRS) Data Release 1 (PanSTARRS DR1; Chambers et al. 2016), and Gaia Data Release 2 (Gaia DR2; Gaia Collaboration et al. 2018b). We applied quality cuts to 2MASS, Pan-STARRS DR1, and Gaia DR2 data, as described in Appendix C, and removed foreground stars using Gaia DR2 parallaxes. We corrected the 2MASS and PanSTARRS photometry in M67 and Ruprecht 147 for extinction using the most recent version (Green et al. 2019) of the dustmaps package that provides 3D dust maps derived from 2MASS and PanSTARRS photometry together with Gaia distances (Green et al. 2018). If there was no Gaia parallax available we used the cluster median distance instead. If an extinction value was not available for a given star we used the average extinction value of the respective cluster. We accounted for extinction in Gaia BP and RP using the reddening  $E(B_P - R_P)$  derived from Gaia photometry and parallax from Gaia DR2 (Andrae et al. 2018). We dropped targets that were too bright and would saturate the detector (Kepler magnitude  $K_p \leq 9$ ).

### 2.3.2. Effective temperatures

We applied several methods and color-temperature relations (CTRs) to determine robust  $T_{\text{eff}}$ . We used CTRs from Boyajian et al. (2013) and Mann et al. (2016) (erratum to Mann et al. 2015),  $T_{\text{eff}}$  derived from Gaia DR2 using the StarHorse algorithm (Queiroz et al. 2018), and  $T_{\text{eff}}$  inferred from Gaia DR2 using the Apsis pipeline (Bailer-Jones et al. 2013; Andrae et al. 2018).

Boyajian et al. (2013) determined CTRs from a range of interferometrically characterized stars using  $g - z$ ,  $g - i$ ,  $g - r$ ,

$g - J$ ,  $g - H$ , and  $g - K$  colors from SDSS and Johnson magnitudes for A to K stars. Their sample was centered on solar metallicity, so we constrained the use of these CTRs to stars with  $-0.25 < [\text{Fe}/\text{H}] < 0.25$ . Following Boyajian et al. (2013), we transformed 2MASS  $JHK$  to  $J - H$ ,  $H - K$ , and  $J - K$  in the Johnson system from 2MASS to the Bessell-Brett system (Carpenter 2001), and from Bessell-Brett to Johnson using the relations in Bessell & Brett (1988).

Mann et al. (2015) derived CTRs from absolutely calibrated spectra to which they fitted atmospheric models to obtain  $T_{\text{eff}}$ . Alternatively, they determined  $T_{\text{eff}}$  from long-baseline optical interferometry measurements using the bolometric flux. They noted transformations for SDSS/2MASS  $r - z$  and  $r - J$ , or Gaia  $BP - RP$  where extra information could be added from metallicity or 2MASS  $J - H$ . The relations in Mann et al. (2015) were only valid if metallicity is sufficiently close to solar, which was satisfied for the OCs in this paper (see Table 1).

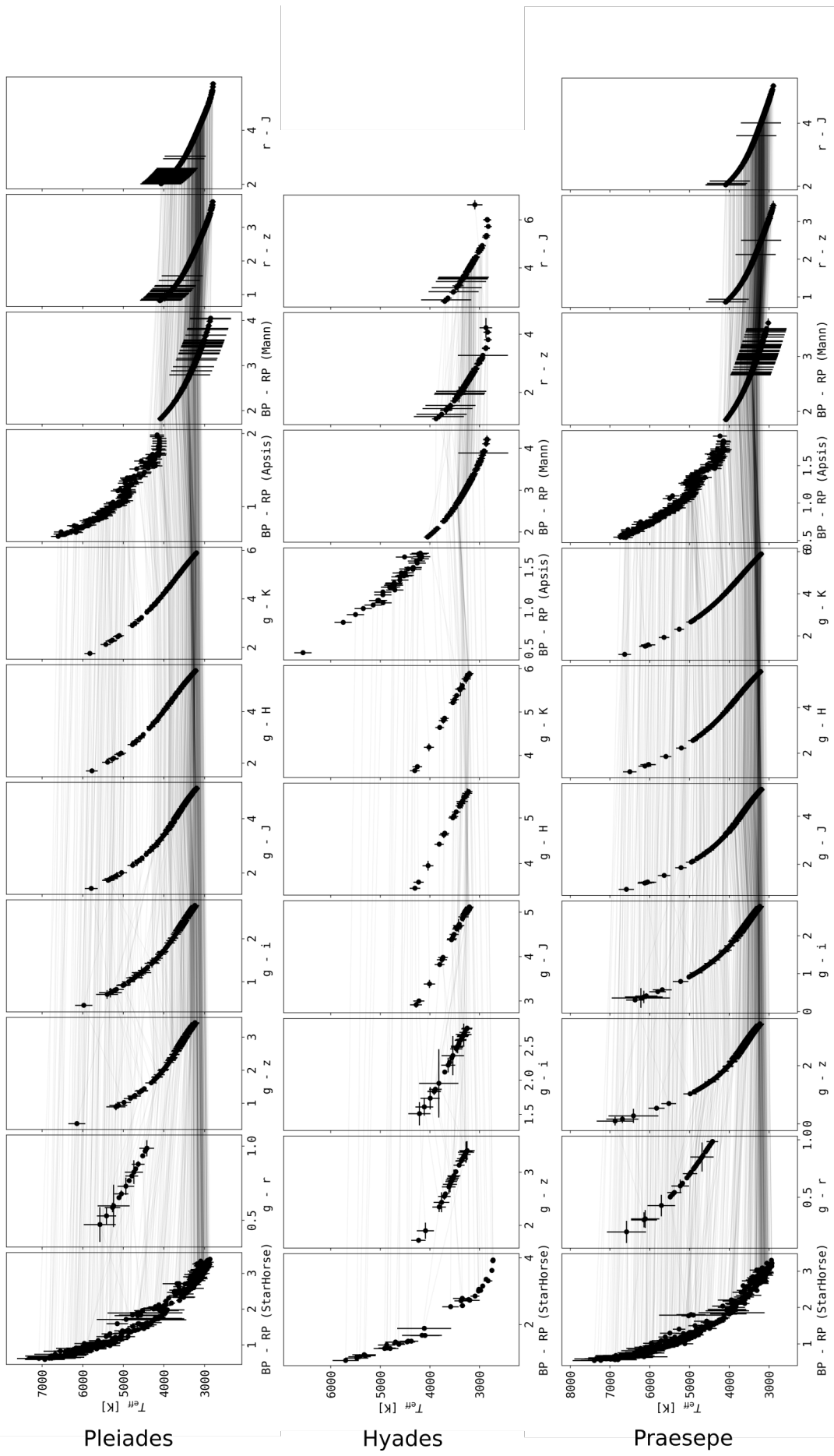
We supplemented our estimates with  $T_{\text{eff}}$  estimates from Anders et al. (2019) who used the StarHorse pipeline (Queiroz et al. 2018) on Gaia DR2.

Gaia DR2 published  $T_{\text{eff}}$  for over 160 million sources (Gaia Collaboration et al. 2018b). The typical uncertainty was quoted at 324 K, but it is lower for stars above  $\sim 4100$  K and below  $\sim 6700$  K, so that we adopt 175 K which is above the quoted root-mean-squared error in this  $T_{\text{eff}}$  range (Andrae et al. 2018), and use provided values only in this range.

Empirical CTRs suffer from systematic errors that stem both from the different methods applied, and from sample selection biases. We therefore used several empirical relations in their appropriate ranges to obtain  $T_{\text{eff}}$  from each, and draw a more reliable median value (Figs. 2 and 3). Targets that were lacking sufficient photometric data to derive  $T_{\text{eff}}$ , or were too hot to be expected to have a convective envelope ( $T_{\text{eff}} \geq 7000$  K), were removed from the sample. We dropped all targets where the uncertainty on the weighted mean  $T_{\text{eff}}$  was greater than 10 %. Only targets that were assigned a  $T_{\text{eff}}$  were searched for flares.

### 2.3.3. Stellar radii

We used a catalog of empirically characterized stars (Yee et al. 2017) and empirical  $T_{\text{eff}} - R_*$  relations derived by Mann et al. (2015, 2016) to obtain  $R_*$  from the  $T_{\text{eff}}$  for the stars in our sample (Fig. 4). Yee et al. (2017) compiled 404 stars with high-resolution spectra from the literature, and performed their own observations of mid to late K-dwarfs, spanning low mass stars from 7000 K down to 3000 K. For these stars, the resulting catalog was accurate to 100 K in  $T_{\text{eff}}$ , 15 % in  $R_*$ , and 0.09 dex in [Fe/H]. We interpolated between stars from the catalog to our de-

**Fig. 2.** Color-temperature relations for Pleiades, Hyades, and Praesepe.

Article number, page 4 of 22

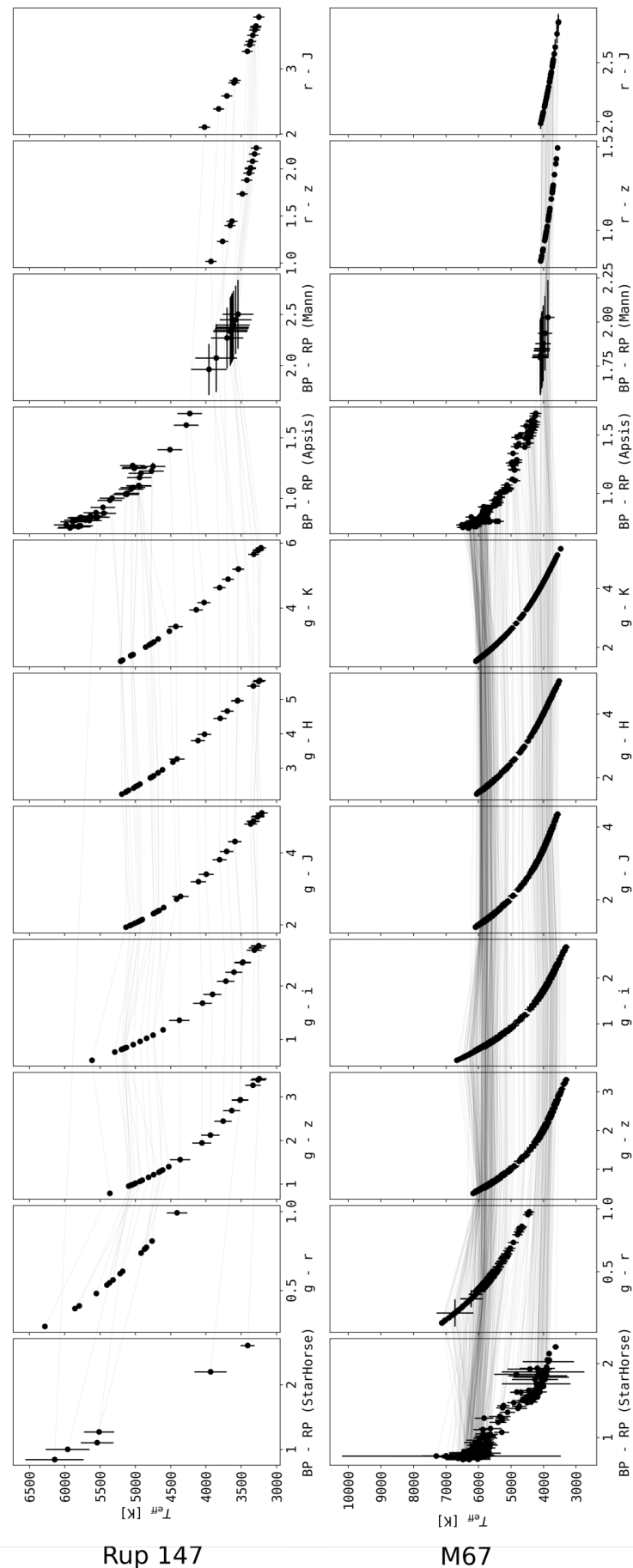


**Fig. 3.** Color-temperature relations for Ruprecht 147, and M67. Description as in Fig. ??.

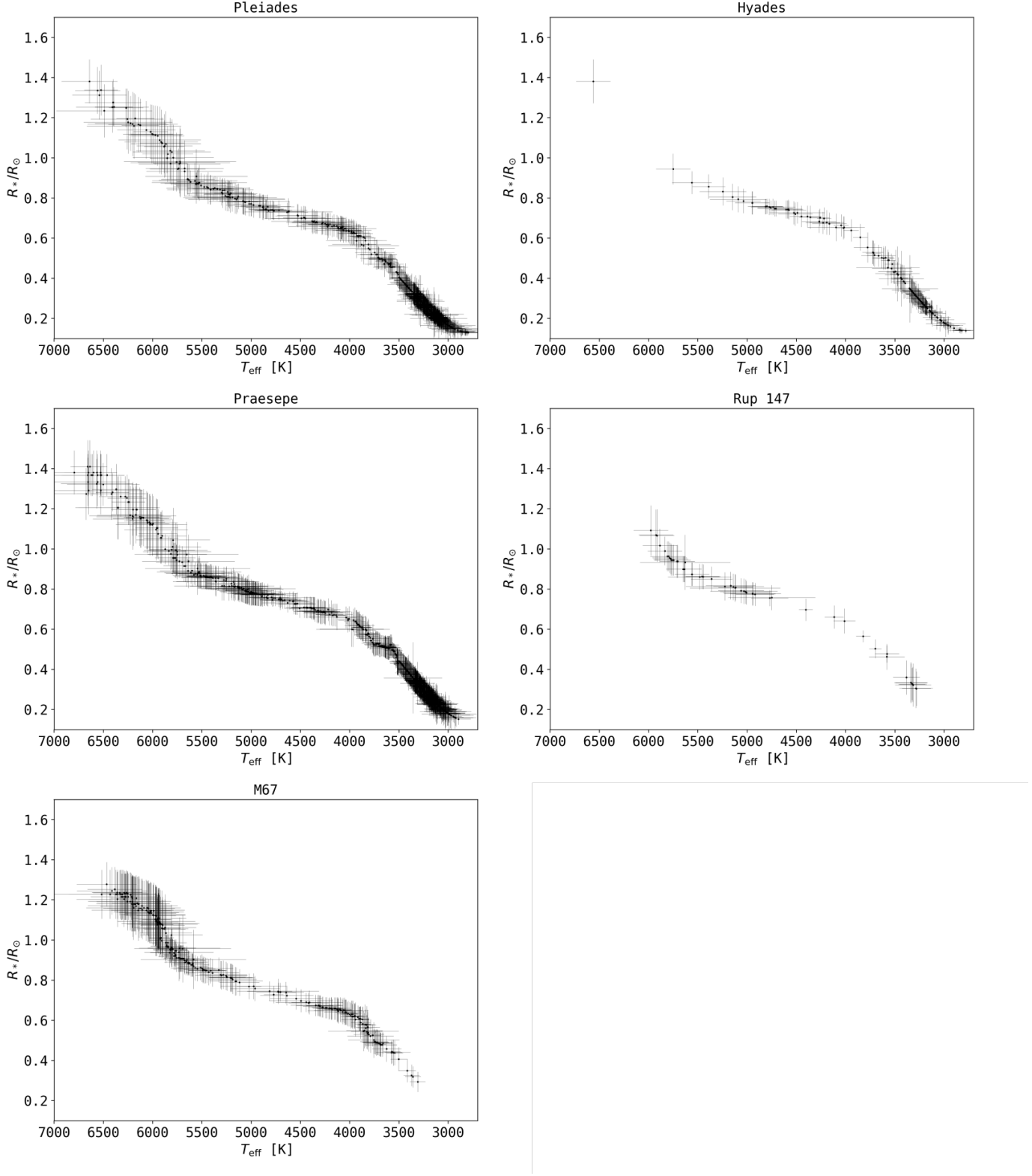


**Fig. 4.**  $T_{\text{eff}}$  –  $R_*$  relation for all clusters in this study.

rived  $T_{\text{eff}}$ , and propagated the resulting scatter to the uncertainty in  $R_*$  if  $T_{\text{eff}} > 3500$  K. For stars with  $T_{\text{eff}} < 3500$  K we used  $T_{\text{eff}} - R_*$  relations derived by Mann et al. (2015, 2016).

#### 2.3.4. Stellar spectra and luminosities

We assigned spectra to our targets from the SpecMatchEmp (Yee et al. 2017) and the FlareSpecPhot libraries (Schmidt 2014; Kirkpatrick et al. 2010; Burgasser et al. 2007, 2008, 2010, 2004; Cruz et al. 2004; Burgasser & McElwain 2006; Rayner et al.

2009; Doi et al. 2010; Filippazzo et al. 2015; Cruz et al. 2003; West et al. 2011; Bochanski et al. 2010, 2007; Schmidt et al. 2010, 2015, 2014; Mann et al. 2015). When a spectrum was available for the derived spectral type in FlareSpecPhot, we preferred it over SpecMatchEmp, which was the case for all stars cooler than M0, where we mapped spectral type to effective temperature as appears in Pecaut & Mamajek (2013). We then combined stellar radii  $R_*$ ,  $T_{\text{eff}}$ , and spectra to projected bolometric luminosities  $L_{\text{bol},*}$ , and projected luminosities in the Kepler band  $L_{\text{Kp},*}$  (Shibayama et al. 2013; Ilin et al. 2019). Uncertainties on  $L_{\text{Kp},*}$  ranged from 9 % to 52 % with a median value of 17 %.

### 3. Methods

We detected flare candidates automatically with the AltaiPony software, and validated them by eye. The frequency distributions of the energies these flares release are believed to follow a power law that spans multiple orders of magnitude. We adopted this model, and fitted the function parameters simultaneously using the Markov Chain Monte Carlo method to sample from the posterior distribution.

#### 3.1. Flare finding

We used the open source software AltaiPony<sup>2</sup> to automatically detect and characterize flares in our sample. The code base relied on K2SC<sup>3</sup> (Aigrain et al. 2016) to remove instrumental and astrophysical variability from K2 light curves. We did not use the de-trended light curves available on MAST<sup>4</sup>, but used K2SC to de-trend light curves from the re-processed final data release. We clipped outliers at  $3\sigma$  iteratively, as compared to the original work, where outliers were clipped at  $5\sigma$  (Aigrain et al. 2016). After de-trending, the flare finder algorithm searched for continuous observing periods, defined as being longer than 10 data points at a minimum cadence of 2 h. All further routines were run on these observing periods. The finder iteratively clipped excursions from the median value at  $3\sigma$  rolling window noise above median plus uncertainty given from K2SC de-trending. After each iteration, outliers were cut down to the current median value. Either after convergence, or 50 iterations, the resulting median value was adopted. With this median as quiescent flux, flare candidates were identified with the same procedure as during the median value calculation, but we additionally required at least three consecutive data points to fulfil the  $3\sigma$ -criterion. Flare candidates were merged into single candidate events if they were less than four data points apart. For each of these candidates flaring time, amplitude and equivalent duration ( $ED$ ) were returned.

$ED$  is the area between the LC and the quiescent flux, that is, the integrated flare flux divided by the median quiescent flux  $F_0$  of the star, integrated over the flare duration (Hunt-Walker et al. 2012):

$$ED = \int dt \frac{F_{\text{flare}}(t)}{F_0}. \quad (1)$$

$ED$  is a quantity independent of calibration and distance that is suited to compare flaring activity on stars where these properties are uncertain.  $ED$  describes the time during which a star releases as much energy as the flare itself. This time can be shorter or

longer than the actual flare duration.

The uncertainty in  $ED$  depended on the light curve noise properties, time sampling, and other intrinsic characteristics. Moreover, K2SC de-trending and the flare finding procedure introduce additional uncertainty that dominates the photometric noise. Computationally, it was too costly to perform the injection and recovery of synthetic flare events to take into account the effects of GP regression that underlies K2SC. Instead we estimated the scatter in the residual flux using the iterative procedure that (Schmidt et al. (2020) in prep.) applied to TESS light curves.

The Kepler flare sample has shown to be difficult to treat in a fully automated way. Without manual vetting, the event samples remain significantly contaminated (Yang & Liu 2019). As K2 was subject to severe technical difficulties, the expected contamination rate was expected to be even higher. Some light curves could not be de-trended using K2SC alone. Light curves with extreme astrophysical signals like deep transits, rotational modulation on time scales of a few hours or passages of bright solar system objects (SSOs) had to be masked accordingly or fitted with an additional sinusoidal component to the K2SC-treated time series. A number of light curves were excluded from the flare search because they saturated the detector, or because the target aperture overlapped with broken pixels. Some very faint targets and extreme variables could not be searched because the de-trending did not terminate successfully. The online version of Table 2 includes an additional flag and contains explanatory notes on the excluded targets.

#### 3.2. Kepler flare energies

Multiband time resolved observations of active M dwarfs have shown that continuum flux accounts for the majority of the energy radiated by flares (Kowalski et al. 2013). The effective temperature of this blackbody, however, varies by a great degree, with, to date, no robust predictor of that temperature: While solar flares are relatively cool, with  $T_{\text{eff}} \approx 5\,000 - 7\,000$  K (Kleint et al. 2016; Kerr & Fletcher 2014; Watanabe et al. 2013; Namekata et al. 2017), SEDs of stellar flares tend to be blue (Davenport et al. 2012). At least one M dwarf flare reached 40\,000 K as seen in FUV spectra (Froning et al. 2019), and most events exhibit temperatures of about 9\,000 – 10\,000 K (Hawley & Fisher 1992; Kretzschmar 2011; Shibayama et al. 2013). A dependence of flare temperature on stellar age, or mass, or both, will enter our analysis if we quantify bolometric flare energy. At about 6\,200 K, the Kepler pass band captures the largest flux fraction, at 10\,000 K 72 %, at 40\,000 K only 4 % of this value is transmitted. A further effect is that flares of equal flare energy but hotter SED would not be seen in the Kepler band at all. Given the uncertainties on stellar luminosity in the Kepler band (see Sec. 2.3.4) and on  $ED$ , the resulting flare energies (PaperI)

$$E_{\text{Kp}} = L_{\text{Kp}} \cdot ED \quad (2)$$

will substantially deviate from the true released energy. If these uncertainties did not affect all flares in a similar fashion, the present analysis will have suffered from non-uniform biases that affected the flare frequency distributions on stars of different ages and temperatures, and skewed the flare distributions within each subsample. However, the comparison to other studies (see Sec. 5.1) suggested that our results were in fact dominated by the astrophysical effects of stellar parameters like mass and age on flare energies and their occurrence rates.

<sup>2</sup> [altaipony.readthedocs.io](https://altaipony.readthedocs.io)

<sup>3</sup> [github.com/OxEs/k2sc](https://github.com/OxEs/k2sc)

<sup>4</sup> [archive.stsci.edu/prepds/k2sc/](https://archive.stsci.edu/prepds/k2sc/)

### 3.3. Power law fits

Flare frequency distributions (FFDs) follow power law relations that cover several orders of magnitude, from solar microflares to stellar superflares. In the cumulative distribution the frequency  $f(> E)$  of flares above a certain energy  $E$  is

$$f(> E) = \frac{\beta}{\alpha - 1} E^{-\alpha+1}. \quad (3)$$

We used and compared two approaches to fitting  $\alpha$  and  $\beta$  to the data. The first was a Modified Maximum Likelihood Estimator (MMLE) for power law distributions (Maschberger & Kroupa 2009). The second approach was more specifically tailored to flaring activity. We used the MCMC method to sample from the predictive distribution for a flare source that produced flares that followed a Poisson process in time, and are power law distributed in the ensemble (Wheatland 2004). While the MMLE was computationally efficient and was useful to obtain first results (see Appendix D), only the predictive distribution allowed us to fit for  $\alpha$  and  $\beta$  simultaneously, and determine their uncertainties.

We adopted the model described in Wheatland (2004). Following their derivation, we defined the joint posterior distribution for the probability  $\epsilon$  that a flare with  $ED$  or  $E_{Kp}$  above some value  $S_2$  would occur within a time period  $\Delta T$ :

$$\begin{aligned} p(\epsilon, \alpha) = & C \cdot (-\ln(1-\epsilon)^M) \\ & \cdot (\alpha-1)^M \cdot \Gamma(\alpha) \left[ \frac{(S_2/S_1)^{M+1}}{\pi} \right]^\alpha \\ & \cdot (1-\epsilon)^{(T/\Delta T) \cdot (S_2/S_1)^{\alpha-1}-1}. \end{aligned} \quad (4)$$

$C$  was the normalisation constant,  $M$  was the number of events,  $T$  the total observation time.  $\Gamma$  contained the prior distribution for  $\alpha$ , and  $S_1$  denoted the detection threshold above which all flares were detected.  $\pi$  encapsulated the flare energies as

$$\pi = \prod_{i=1}^M \frac{s_i}{S_1}, \quad (5)$$

where  $\{s_1, s_2, \dots, s_m\}$  were the flare energies  $E_{Kp}$  or  $ED$ .

The posterior distribution in Wheatland (2004) captured both the Poissonian distribution of flare events in time, and their power law distribution in energy, simultaneously. The authors derived this model to be able to predict the flaring rate above a given energy for any active region on the Sun, and offered an extension to Eq. 4 that treated changing flaring activity rates as the active region evolves, and also characteristics of the active region itself, such as sunspot classifiers. In the above simplification of the model, we assumed that the flare generating process did not change within the observation time span in any star in our sample ( $M = M'$  in Eq. 24 in Wheatland (2004)). Another assumption was that this process was the same for all stars in the sample ( $\Lambda_{MC} = 1$  in aforementioned Eq. 24). Under these assumptions the samples of flares found in the light curves of different stars and light curves obtained during different campaigns could be stacked together.

From the posterior distribution of  $\epsilon$  we derived  $\beta$  by combining Poisson statistics

$$\epsilon = 1 - e^{(-f \cdot \Delta T)} \quad (6)$$

and the cumulative power law function in Eq. 3:

$$\beta = -\frac{\ln(1-\epsilon) \cdot (\alpha-1)}{\Delta T} \cdot S_2^{\alpha-1} \quad (7)$$

With a uniform prior for  $\alpha$  the results from the MLE and Markov Chain Monte Carlo (MCMC) sampling from the posterior distribution were consistent within uncertainties (see Appendix D). However, the MCMC method allowed us to fit for both  $\epsilon$  and  $\alpha$  simultaneously, and to use more informative priors.

The power law exponent determined for flare frequency distributions has consistently been found to be independent of age (Davenport et al. 2019), and spectral type for solar-type and low mass dwarfs (see Fig. F.1 in Appendix F). We chose our prior to reflect this result: Starting from a uniform prior for  $\alpha$  and  $\epsilon$ , we found a Gaussian distribution to be an excellent fit to the posterior distribution for  $\alpha$  for the full sample of flares in  $E_{Kp}$  and  $ED$  space. We then used this Gaussian distribution as a prior for the FFDs in individual age and  $T_{\text{eff}}$  bins.

## 4. Results

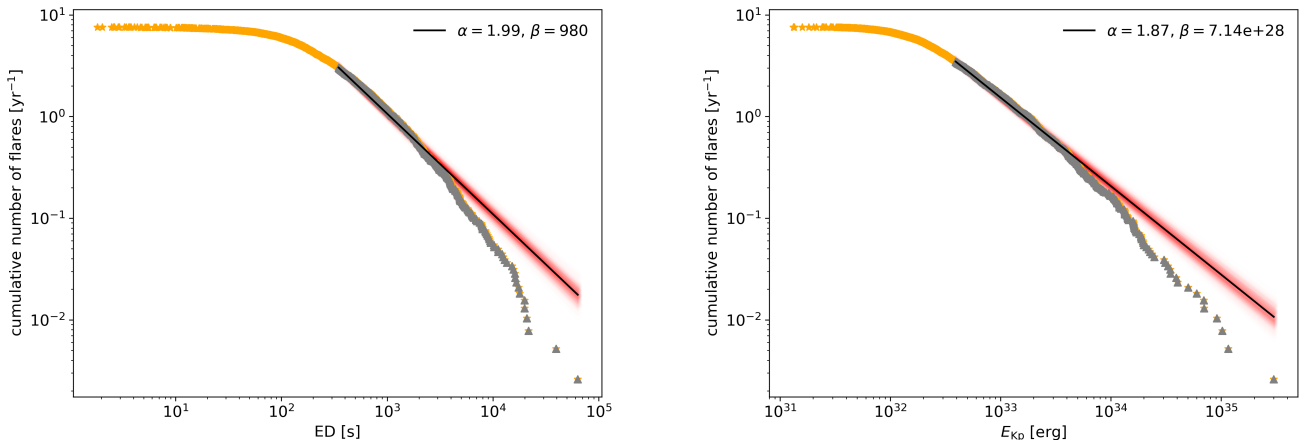
The core objective of this work was to quantify how the decline in flaring activity with age unfolds for different spectral types. To this end, we searched the long cadence light curves of stars across a broad range of spectral types in five different open clusters for flares, and measured their energies and occurrence rates. We found 2918 flares. We then fitted power law relations to the flare frequency distributions (FFD) of samples of stars split up by cluster, that is, age, and effective temperature bins, that is, spectral type. We found that flaring activity dropped significantly with increasing age from ZAMS to 3.6 Gyr, and from mid-M to G dwarfs. Except for the stars in the coolest temperature bin (M5.5-M8, 2 500-3 000 K), stellar flaring activity at a given age was higher for a cooler star.

### 4.1. Flare frequency distributions

We fitted power law parameters for  $\alpha$  and  $\beta$  to the full sample FFDs in  $E_{Kp}$  and  $ED$  space by sampling from the joint posterior distribution in Eq. 4. We chose uninformative priors for both  $\alpha$  and  $\epsilon$ . The detection threshold in any FFD is not a unique function of  $E_{Kp}$  or  $ED$ , but depends on the flares' amplitudes and durations. Since it was computationally not feasible to perform the injection of synthetic flares to determine the effect of K2SC de-trending, we must acknowledge the incompleteness of flare detection at the low energy end. To a first approximation to a detection threshold, we chose to use only the portion of the FFD for the fit, where all flaring stars contribute, that is where all contributing stars will have exceeded the detection threshold. This mitigated but did not solve the problem of a detection probability  $< 1$  that still affected the shape of the FFDs at the lower energy end. It was no solution, however, to exclude even more flares on the low-energy, because then the high-energy tail gains increasing weight. In the case of the full sample we expect that for some stars the high-energy threshold will be reached at some energy below the maximum detected energy in the sample. Consequently the high-energy tail of the FFD will also be incomplete. To arrive at consistency with a powerlaw at a 5% significance level using a Kolmogorov-Smirnov as suggested by Wheatland (2004) by choosing ever higher low-energy cutoffs, we would have had to exclude the majority of flares. The power law exponent in these cases would have approached  $\alpha \sim 2.4$  (using only about 320 flares out of 2918). The absolute value of  $\alpha$  in this work is therefore of limited significance. It remains useful as a relative anchor for the comparison within the sample because the FFDs for different age and  $T_{\text{eff}}$  bins suffer from the same incompleteness. Making use of this, we fitted a Gaussian distribution to the posterior distribution for  $\alpha$  from the full sample and took

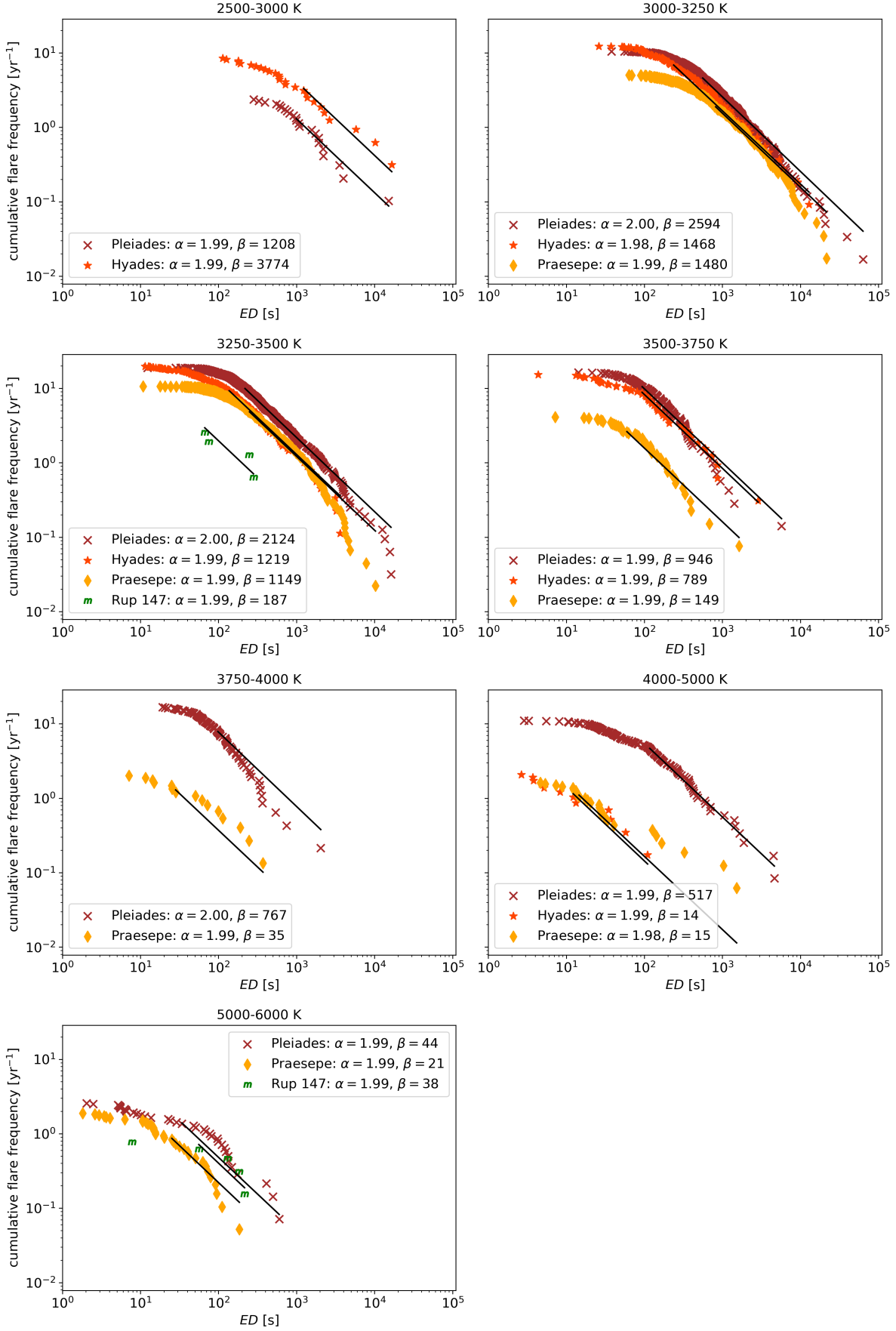
**Table 2.** Selection of confirmed flare candidates detected in open clusters observed by Kepler/K2, sorted by amplitude  $a$ . The full table is available on CDS. Uncertainties are noted in parentheses.

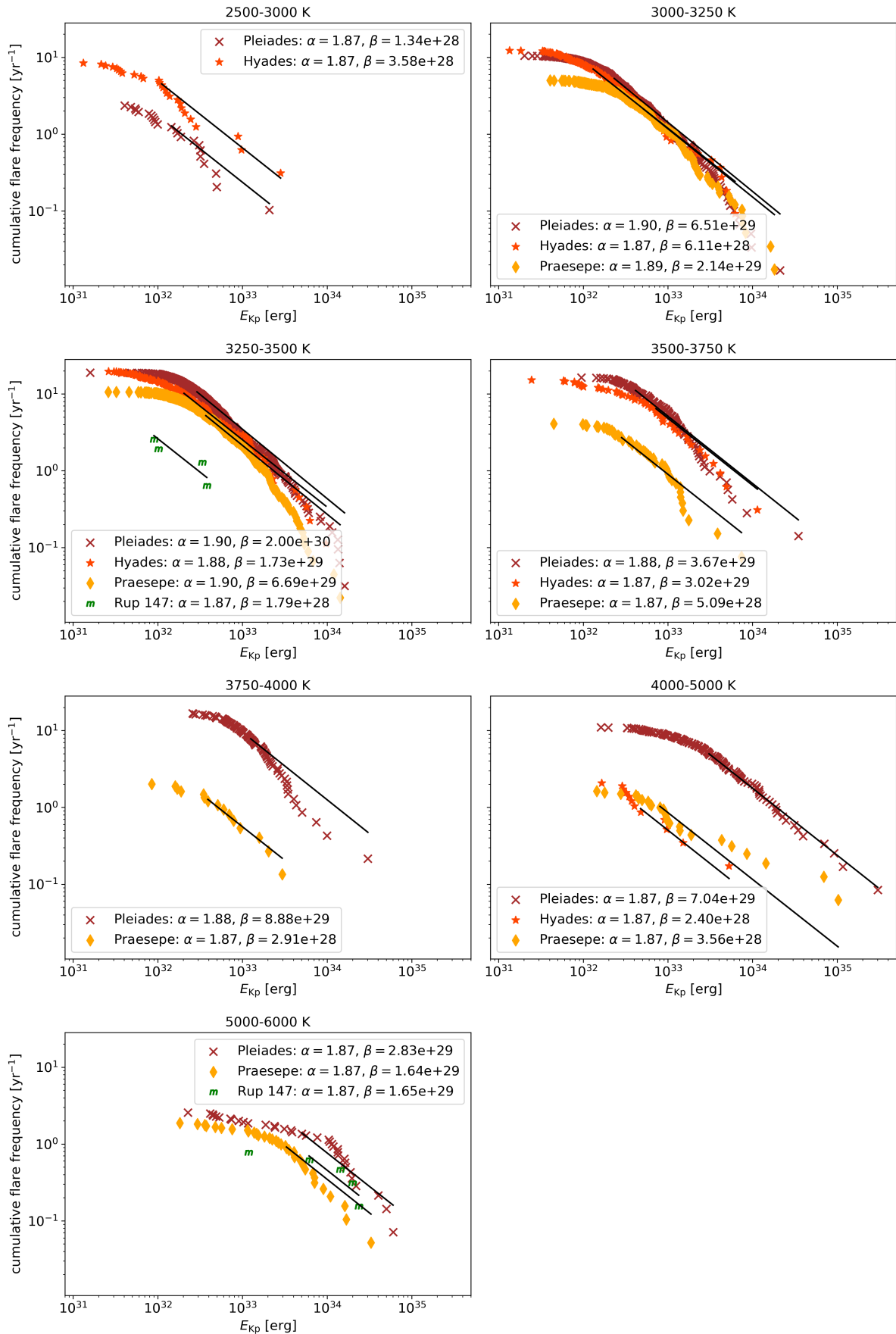
EPIC	C	cluster	$c_0$	$c_1$	$a$	$T_{\text{eff}}$ [K]	$ED$ [s]	$L_{\text{bol},*}$ [erg/s]	$L_{\text{Kp}}$ [erg/s]
211079830	4	Pleiades	105984	105993	15.330194	3097(87)	63340(63)	$8.29(3.34)10^{29}$	$3.32(1.34)10^{29}$
210720772	4	Pleiades	107181	107184	9.674757	3104(86)	19901(7)	$8.66(3.45)10^{29}$	$3.48(1.38)10^{29}$
247523445	13	Hyades	143106	143109	8.260956	2964(49)	16615(11)	$4.33(1.09)10^{29}$	$1.69(0.43)10^{29}$
212021131	5	Praesepe	108974	108980	7.421916	3215(68)	19828(175)	$2.01(0.65)10^{30}$	$8.22(2.65)10^{29}$
210978953	4	Pleiades	106762	106770	6.769888	3050(95)	39467(125)	$6.20(2.63)10^{29}$	$2.46(1.04)10^{29}$
211913613	16	Praesepe	156845	156849	6.690356	3218(66)	21632(147)	$2.05(0.65)10^{30}$	$8.37(2.63)10^{29}$
211127297	4	Pleiades	106754	106759	6.449569	3147(86)	20830(5)	$1.13(0.45)10^{30}$	$4.59(1.81)10^{29}$
211681193	5	Praesepe	108116	108120	5.570804	3182(76)	11198(95)	$1.64(0.58)10^{30}$	$6.68(2.37)10^{29}$
211024798	4	Pleiades	104822	104826	5.394897	3290(62)	12524(63)	$2.58(0.75)10^{30}$	$1.06(0.31)10^{30}$
211134185	4	Pleiades	103891	103896	4.951629	3127(96)	17459(33)	$9.99(4.33)10^{29}$	$4.03(1.75)10^{29}$
211095280	4	Pleiades	106283	106287	4.796979	3138(93)	12186(10)	$1.06(0.45)10^{30}$	$4.32(1.82)10^{29}$
211022535	4	Pleiades	104262	104267	3.994973	2953(76)	15164(57)	$3.50(1.10)10^{29}$	$1.37(0.43)10^{29}$
211010517	4	Pleiades	106680	106685	3.968907	3252(70)	16241(171)	$2.09(0.68)10^{30}$	$8.59(2.77)10^{29}$
210846442	4	Pleiades	104410	104415	3.959977	3311(79)	13515(10)	$2.88(0.96)10^{30}$	$1.18(0.40)10^{30}$
212017838	5	Praesepe	111183	111192	3.671037	3307(89)	10274(10)	$3.35(1.22)10^{30}$	$1.38(0.50)10^{30}$
211984058	5	Praesepe	109952	109965	3.320636	3124(97)	16063(149)	$1.17(0.51)10^{30}$	$4.73(2.06)10^{29}$
211912899	5	Praesepe	110700	110706	3.257997	3133(81)	7967(16)	$1.24(0.47)10^{30}$	$5.01(1.89)10^{29}$
211151674	4	Pleiades	106457	106467	3.166323	3072(93)	17843(106)	$7.10(2.99)10^{29}$	$2.84(1.19)10^{29}$
211822895	5	Praesepe	107809	107812	3.164494	3005(177)	6883(31)	$5.68(3.98)10^{29}$	$2.25(1.57)10^{29}$
211760567	5	Praesepe	109962	109965	3.061417	3245(58)	7838(9)	$2.39(0.69)10^{30}$	$9.84(2.83)10^{29}$
211939350	16	Praesepe	155018	155022	2.892939	3149(150)	9542(68)	$1.36(0.86)10^{30}$	$5.52(3.49)10^{29}$
211137806	4	Hyades	106768	106775	2.482828	3127(58)	9208(8)	$1.16(0.35)10^{30}$	$4.69(1.40)10^{29}$
210674207	13	Hyades	141708	141711	2.419586	3210(74)	5343(3)	$1.90(0.65)10^{30}$	$7.78(2.66)10^{29}$
211994910	5	Praesepe	109858	109864	2.401426	3235(95)	7807(14)	$3.71(1.40)10^{30}$	$1.53(0.58)10^{30}$
211010517	4	Pleiades	106561	106564	2.341076	3252(70)	4838(36)	$2.09(0.68)10^{30}$	$8.59(2.77)10^{29}$
211984058	5	Praesepe	108584	108587	2.155468	3124(97)	4817(13)	$1.17(0.51)10^{30}$	$4.73(2.06)10^{29}$
211983544	18	Praesepe	162792	162798	2.096077	3159(98)	6924(55)	$1.44(0.63)10^{30}$	$5.88(2.55)10^{29}$
210988354	4	Pleiades	106012	106017	2.057812	3661(144)	5725(1)	$1.40(0.31)10^{31}$	$6.06(1.32)10^{30}$
210886447	4	Pleiades	103871	103877	2.057490	3048(105)	8710(49)	$6.13(2.83)10^{29}$	$2.43(1.12)10^{29}$
211098921	4	Pleiades	105254	105262	2.041041	3300(101)	7499(5)	$2.72(1.10)10^{30}$	$1.12(0.45)10^{30}$

**Fig. 5.** FFD (scatter) in  $ED$  (left panel) and energy (right panel) and respective power law fit (black line) to the full sample of flare candidates. The full FFD is shown in orange, the portion used for the fit is overplotted in grey. The red shade is a randomly drawn sample from the posterior distribution.

it as a prior for the power law fits to the FFDs in the individual bins. The values for the full sample FFDs in  $E_{\text{Kp}}$  and  $ED$  space (Fig. 5) are summarized in Table 4. The core part of this work was to investigate the effects of age on the flaring activity for low mass stars. We therefore split up the full sample into  $T_{\text{eff}}$  bins and constructed the FFDs cluster by cluster (Figs. ??, and ??). The power law fit parameters to these FFDs are summarized in Table 3. To this end, the flaring activity

was best described by the  $\beta_s$ , the power law fit intercept for the FFDs in  $ED$  space. It accounted for the different energy budgets of stars, by looking at the relative flare energies as measured by  $ED$  as opposed to  $\beta_{\text{erg}}$  which was based the Kepler band flare energy  $E_{\text{Kp}}$ . We could therefore use  $\beta_s$  to compare across both  $T_{\text{eff}}$  and age. Overall,  $\beta_s$  declined with age in all investigated  $T_{\text{eff}}$  bins but the 2500 – 3000 K bin, where it increased from ZAMS to Hyades age (Fig. 8).

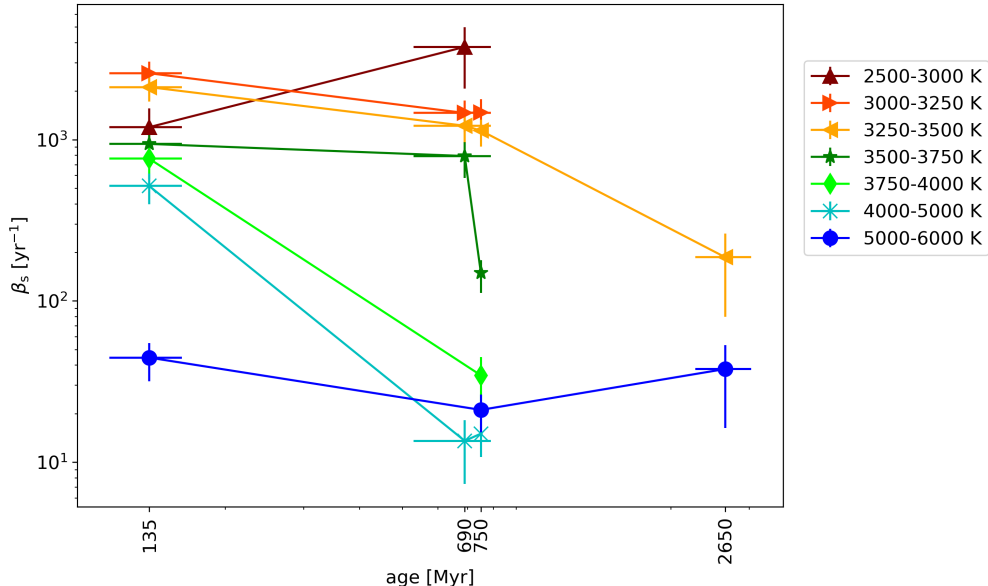
**Fig. 6.** FFDs (scatter) in ED and respective power law fits (black lines).



**Fig. 7.** FFDs (scatter) in  $E_{\text{Kp}}$  and respective power law fits.

**Table 3.** Summary of flaring  $\beta$  of all clusters and  $T_{\text{eff}}$  bins in  $E_{\text{Kp}}$  and  $ED$  distributions.

		$\alpha_s$	$\beta_s$	$n_s$	$\alpha_{\text{erg}}$	$\beta_{\text{erg}}$	$n_{\text{erg}}$
2500-3000	Hyades	1.99 (0.03)	3757 (1688) 1222	27	1.87 (0.02)	0.4 (1.9) 0.3	10 <sup>29</sup>
	Pleiades	1.99 (0.03)	1193 (500) 370	23	1.87 (0.02)	1.3 (6.5) 1.1	10 <sup>28</sup>
3000-3250	Hyades	1.98 (0.03)	1462 (353) 285	133	1.87 (0.02)	0.6 (2.8) 0.5	10 <sup>29</sup>
	Pleiades	2.00 (0.03)	2581 (569) 466	623	1.90 (0.02)	0.6 (2.4) 0.5	10 <sup>30</sup>
3250-3500	Praesepe	1.99 (0.03)	1475 (385) 306	289	1.89 (0.02)	2.0 (9.4) 1.7	10 <sup>29</sup>
	Hyades	1.99 (0.03)	1218 (262) 218	175	1.88 (0.02)	1.8 (8.1) 1.5	10 <sup>29</sup>
3500-3750	Pleiades	2.00 (0.03)	2116 (396) 334	598	1.90 (0.02)	2.0 (7.9) 1.6	10 <sup>30</sup>
	Praesepe	1.99 (0.03)	1137 (233) 189	477	1.89 (0.02)	0.6 (2.6) 0.5	10 <sup>30</sup>
3750-4000	Rup 147	1.99 (0.03)	186 (106) 74	4	1.87 (0.02)	1.8 (9.0) 1.5	10 <sup>28</sup>
	Hyades	1.99 (0.03)	790 (213) 173	49	1.87 (0.02)	3.0 (14.9) 2.5	10 <sup>29</sup>
4000-5000	Pleiades	1.99 (0.03)	940 (198) 166	116	1.88 (0.02)	0.4 (1.7) 0.3	10 <sup>30</sup>
	Praesepe	1.99 (0.03)	148 (36) 30	54	1.87 (0.02)	0.5 (2.5) 0.4	10 <sup>29</sup>
5000-6000	Pleiades	2.00 (0.03)	762 (192) 155	78	1.88 (0.02)	0.9 (4.3) 0.7	10 <sup>30</sup>
	Praesepe	1.99 (0.03)	34 (13) 10	15	1.87 (0.02)	3.0 (14.8) 2.5	10 <sup>28</sup>
4000-5000	Hyades	1.99 (0.03)	13 (6) 4	12	1.87 (0.02)	2.4 (12.3) 2.0	10 <sup>28</sup>
	Pleiades	1.99 (0.03)	516 (119) 98	131	1.87 (0.02)	0.7 (3.4) 0.6	10 <sup>30</sup>
5000-6000	Praesepe	1.98 (0.03)	15 (4) 3	26	1.87 (0.02)	0.4 (1.8) 0.3	10 <sup>29</sup>
	Pleiades	1.99 (0.03)	44 (12) 10	36	1.87 (0.02)	2.8 (14.4) 2.4	10 <sup>29</sup>
5000-6000	Praesepe	1.99 (0.03)	21 (6) 5	36	1.87 (0.02)	1.7 (8.6) 1.4	10 <sup>29</sup>
	Rup 147	1.99 (0.03)	37 (21) 15	5	1.87 (0.02)	1.6 (9.2) 1.4	10 <sup>29</sup>

**Fig. 8.** Flare  $\beta_s$  vs. age grouped by  $T_{\text{eff}}$ .**Table 4.** Summary of FFD parameters and power law fits to the full sample of all clusters in  $E_{\text{Kp}}$  and  $ED$  space.  $n_{\text{tot}}$ : number of flares in the FFD.  $n_{\text{fit}}$ : number of flare used to fit the power law.

	$ED$	$E_{\text{Kp}}$
$\alpha$	1.99 (0.03)	1.87 (0.02)
$\beta$ [yr <sup>-1</sup> ]	980 (216) 178	7.14 (36.87) 5.98
$n_{\text{tot}}$	2913	2913
$n_{\text{fit}}$	1166	1336

#### 4.2. Flaring luminosity FA

The energy released in flares was inferred using our derived stellar luminosities. It declines with age for every  $T_{\text{eff}}$  bin considered for both the total luminosity and relative to the quiescent flux (Fig. ??).

$L_{\text{Kp,flare}}$  is the luminosity in flares in the Kepler band. We can relate this to the quiescent bolometric luminosity of the star when

**Table 5.** Mass budget of flaring stars in M67 and Rup 147 within uncertainties on radius. The hypothetic binary pairs were calculated assuming that the primary mass was the smallest possible within  $1\sigma$  of the uncertainty on their radii. Median SpT: The spectral type of the target if it was a single star. Binary: The hypothetic binary pair with the highest possible mass ratio.

EPIC	median SpT	binary
211434440	K1	K2 + M5.5
219601739	G8	K1 + M6
219610232	K0.5	K2 + M5.5
219591752	M3	M3.5 + M3.5

we define the fractional flare luminosity  $FA$  in analogy to PaperI:

$$FA = \frac{E_{Kp,\text{flare,tot}}}{t \cdot L_{\text{bol},*}}, \quad (8)$$

We determined  $L_{\text{bol},*}$  from  $R_*$  and  $T_{\text{eff}}$ , as described in Sec. 2.3. In Fig. ?? we computed the median and standard deviation  $FA$  for every  $T_{\text{eff}}$  bin.  $FA$  is a meaningful measure of relative stellar activity as long as the flux portion of the quiescent star in the Kepler band is roughly constant. It is therefore more meaningful to compare  $FA$  values across age than across  $T_{\text{eff}}$ .

#### 4.3. Hyades and Praesepe

We expected the flaring activity in the Hyades and Praesepe to be very similar because they were nearly coeval clusters with ages around 700 Myr, and comparable metallicities ([Fe/H](Praesepe) = 0.16, [Fe/H](Hyades) = 0.13, Netopil et al. 2016). We found this reflected in all our FFDs, except for the 3500 – 3750 K temperature bin, where the Hyades appeared almost as active as the Pleiades (135 Myr). This discrepancy could be explained by the rotation period distributions of their samples. In all other temperature bins the rotation period distributions of the Hyades and Praesepe were similar, while the Pleiades showed shorter periods on average. In the 3500 – 3750 K temperature bin, the rotation periods found in the Hyades and the Pleiades were more alike than in the Hyades and Praesepe (see Fig. E.1 in the Appendix). In this temperature regime, the overwhelming majority of Praesepe stars had rotation periods above 10 d, while in the Hyades and the Pleiades rotation periods were more evenly distributed in the 0.3 – 30 d range.

#### 4.4. M67 and Rup 147

We found several flare candidates in members of M67 and Rup 147. But upon close inspection all but the events that occurred on four stars either turned out to be false positives (SSOs), or the stars were multiples or evolved stars. Most flare candidates in these old clusters were detected on RS CVn binaries, cataclysmic binaries, Algol type binaries, spectroscopic and eclipsing binaries, and red giant stars. Excluding all these, we were left with one flare in M67 on a K1 dwarf. In Rup 147, we narrowed down the list to a flare on a G8 star in Rup 147, and four flares each on a K0.5 and an M3 star. For these stars, the multiplicity status was unknown. We found that the mass range of these stars as calculated from the uncertainties on their radii (Eker et al. 2018) was large enough that the four stars in question could in principle be binary stars with undetected mid-M dwarf companions (Table 4.4). While binaries and false positives were present in the younger clusters also, they were not the dominating source of flares.

## 5. Discussion

### 5.1. Consistency with other studies

EvryFlare, mass-dependence,

### 5.2. M37

Comparing our results to a similar study of photometric flares in M37 (Chang et al. 2015) we find the results somewhat discrepant. M37 is 300–600 Myr old and appears less active than Praesepe and Hyades in individual Teff bins, which are of coeval or older. We attribute the difference to the loose membership requirement of  $pmem \geq 0.2$  in Chang et al. (2015) as compared to our stricter cuts at 0.8. We expect the M37 to be contaminated with field stars that systematically reduce the flaring rates. Applying our own restriction the M37 sample (Chang et al. 2016) leaves very few flares that hamper a statistical description of their distributions.

### 5.3. Division at 3000 K

The lowest  $T_{\text{eff}}$  bin at Pleiades age in our sample reflects the division between fully convective stars and those with a radiative core (Reid & Hawley 2005). At this age, the coolest dwarfs may still be accreting angular momentum on the PMS, instead of spinning down on the MS. We suggest that a regime change occurs around 120 Myr for stars with  $T_{\text{eff}} = 2500 – 3250$  K. Below 3000 K, an analysis of 66 ZDI maps show that magnetic field configurations can be strong and dipolar or weak and multipolar (Morin et al. 2008; See et al. 2017). If these stars can be distinguished by age, this should be reflected in our age-resolved flaring activity. If the difference is not a function of age, we should see a similar bimodal distribution of very inactive and very active stars in the lowest mass bins. If the difference between the two configurations is a function of age, we should only see one type of stars with correspondingly similar behaviour in these  $T_{\text{eff}}$  bins.

The lowest mass bin appears underactive compared to the rest of the flaring-age- $T_{\text{eff}}$  relation in the  $ED$  domain. Physical explanations for this peculiarity include: A different magnetic structure A truncation of the power law that reflects the maximum  $ED$  an active region can produce on these stars.

West et al. (2015) found that all M1–M4 dwarfs with rotation periods shorter than 26 days, and all M5–M8 dwarfs with periods shorter than 86 days show H $\alpha$  emission, indicating their magnetic activity.

Assuming a typical binary fraction for early and mid M dwarfs (Fischer & Marcy 1992), we can expect some of the flares on stars at  $T_{\text{eff}} > 3000$  K to belong to unresolved binary companions with  $T_{\text{eff}} < 3000$  K. A misattributed flare on an early M dwarf then will be assigned a too small  $ED$ , but still a correct  $E_{Kp,\text{flare}}$  because the count ratios are equal to the  $L_{Kp}$  ratios.

### 5.4. Comparison to other work

Davenport et al. (2019) note a sample bias towards more active stars. Their models overpredicts the superflaring rate of the average Sun-like sample from Shibayama et al. (2013) and more resembles the rate for their most active sub-sample.

The frequency of superflares at  $10^{34}$  erg in the most active G-dwarfs and Sun-like stars in Kepler was once in 10–100 days, and every 800 years on average Sun-like stars (Shibayama et al. 2013). Benchmarking on the flare detected on a K1 dwarf in M67

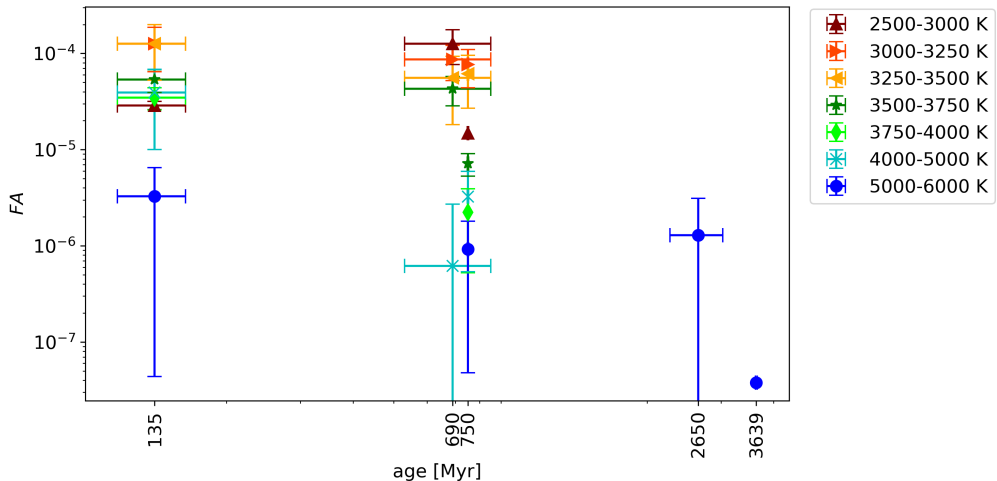


**Fig. 9.** FA for flares above the shared energy threshold ( $3.98 \cdot 10^{32}$  erg) as determined for the full FFD in  $E_{Kp}$  in Fig. 5.

in the G to early K bin (5000-6000 K), and accounting for the fraction of the total flare energy that the Kepler passband covers at a flare temperature of 10 000 K, we found the flaring rate at this energy to amount to about once every 10 years. Doing the same for the Pleiades stars yielded that ZAMS G to K dwarfs flare once in 140 days at  $10^{34}$  erg.

Compare to other FFD values, e.g., from Ward's Evryscope survey, see table in Appendix, and maybe convert it to a plot Howard et al (2019) monitored superflares on cool stars with bolometric energies above  $10^{33}$  erg and up to  $10^{36}$  erg. They find power law exponent values around  $\sim 2$  resolved by spectral types. Similar values are found for individual flare stars (Lurie et al. 2015).

Howard+18, Loyd+18, Tilley+19 show that flares can erode exoplanetary atmospheres. If a flare is assumed to deposit its UV energy in an instant a single superflare can completely remove the ozone layer at the substellar point Loyd+18. Associated protons are safer way to ozone destruction if they are associated with reoccurring large flares Tilley+19

Raetz et al. (2020) pointed out that their fast rotators appeared were more active than my Pleiades sample

### 5.5. Universality of $\alpha$

It was not straightforward to account for the deviation from an ideal power law. At both low and high energies, the detection was incomplete.

At the low-energy end the detection probability depended on flare duration and amplitude. These parameters were not resolved in FFDs, and while they are correlated there is significant spread in the duration-amplitude relation to blur the cutoff in the FFD. One way to account for this circumstance is to inject and recover synthetic flares with a variety of durations and amplitudes and to determine energy ratios and recovery probabilities for each flare candidate, assuming that the underlying flare shape can be sufficiently well parametrized. This was first explored in Davenport et al. (2014) for Kepler data and expanded in (Schmidt et al. 2020) for TESS. However, GP regression, which was used to de-trend the light curves, was in itself too costly to repeat it hundreds of times for each light curve.

At the high energy end, the incompleteness is most likely to occur in the full sample FFDs where we expect maximum energy thresholds to be reached for certain spectral types and ages.

These effects may be partly cancelled by background contami-

nation from, for instance, cosmic rays (Aschwanden 2015), or solar system objects (SSO). We were also limited by the non-linear dependence for the energy bias from time sampling effects that lead to the severe underestimation of flares energies, as can be observed by comparing flare energies derived for the same flare events from short and long cadence light curves (Yang et al. 2018).

Taking into account uncertainties and systematic errors resulting power law fitting methods, the power law exponent  $\alpha \sim 2$  appeared to be similar for the majority of studies on flare statistics in the literature so far, irrespective of spectral type or age. The values derived for  $\alpha$  in our sample were almost precisely 2 in  $ED$  space, and somewhat below 2 in  $E_{Kp}$ , consistent with previous work.

### 5.6. Deviations from single power law

Full sample is not consistent with a power law while the subsamples for different effective temperatures and ages mostly are. This can be interpreted as ..

Spots can survive on the stellar surface from a few days to nearly a year (Namekata et al. 2017; Davenport 2015). Namekata et al. (2017) find conceivable that spots evolve on timescale shorter than the estimated lifetimes. Complex spot geometry is correlated with the strongest X-class flares on the Sun (Toriumi et al. 2017; Sammis et al. 2000). This supports the idea that flares are associated with the presence of certain types of starspots, or more generally, certain types of active regions. Since we can reasonably expect that there is a maximum flare energy a spot can produce, the underlying power law relation must break at some  $ED_{\max}$ . We tested a possible truncation of our FFDs, but find no conclusive evidence for it in any FFD with  $> 50$  data points. As we stack multiple targets, each potentially with multiple, evolving spots of various sizes on their surfaces, into one FFD at a time, we might observe a deviation but no truncation. A different explanation is simply that we do not sample the maximum energies, as extremely high relative fluxes have been observed in the past (Paudel et al. 2018; Jackman et al. 2019; Schmidt et al. 2016).

## 6. Summary and Conclusions

*Is there or will be there more data available to further extend the sample?* There are no model-independent stellar ages. It is more correct to speak of evolutionary stage. Stars in open clusters with precise isochronal ages have their observables reduced to a number of years. We can now ask: Can we unambiguously map flaring evolutionary stage to the evolutionary stage of isochronal fit parameters of a given star? If there is either a strong correlation, or even a physical relation between flaring activity and, for instance, mass and rotation rate, the answer is yes. If this relation is sufficiently sensitive to be captured by present day instrumentation, and non-degenerate in the relevant parameters, flaring activity can be integrated into the family of age indicators, and complement and extend them.

Ultimately, flaring activity depends on how efficiently the star converts its energy budget to flares throughout its lifetime. Since the fraction of total luminosity released in flares is small even for the most active stars, this efficiency need not scale directly with the overall energy budget of the star on the MS, but will more likely depend on the ability of the star to use this budget to produce magnetic surface topologies and strengths that enable flaring.

A magnetic dynamo, driven by rotation and convection, introduces magnetic field to the system that causes stellar wind that in turn removes angular momentum from the star, decreasing its rotation rate. Over time, the wind takes away more and more angular momentum, and the global magnetic field weakens. This is reflected in observations of chromospheric indicators (ZDI???). The decline is famously known as the Skumanich law, and gave rise to the rotational age-dating technique called gyrochronology. However, recent studies noted deviations from this rule, a stalling of the spin-down, and offered multiple competing explanations. It is not clear how these effects reflect on the small scale surface magnetic field. Chromospheric activity on solar type stars seems to continue to decline regardless of these rotational effects.

What about X-ray?

Observationally, not much can be directly said about the small scale topology of stellar magnetic fields beyond extrapolations from the solar case. On the Sun, chromospheric activity indicates line emission in excess of radiative equilibrium that is caused by magnetic fields. Likewise, magnetic field effects heat the corona

**Acknowledgements.** This work made use of the `gaia-kepler.fun` crossmatch database created by Megan Bedell. Kepler-affiliated tools were used in the process: `lightkurve`, `K2SC`, `AltaiPony`. Also: `numpy`, `pandas`, `astroml`, `astropy`, `specmatch-emp`, `bokeh` (Bokeh Development Team 2019)... `TOPCAT`: This research made use of the cross-match service provided by CDS, Strasbourg. This work has made use of data from the European Space Agency (ESA) mission `Gaia` (<https://www.cosmos.esa.int/gaia>), processed by the `Gaia` Data Processing and Analysis Consortium (DPAC, <https://www.cosmos.esa.int/web/gaia/dpac/consortium>). Funding for the DPAC has been provided by national institutions, in particular the institutions participating in the `Gaia` Multilateral Agreement. If you have used `Gaia` DR2 data in your research, please cite both the `Gaia` mission paper and the `Gaia` DR2 release paper: `Gaia` Collaboration et al. (2016): Description of the `Gaia` mission (spacecraft, instruments, survey and measurement principles, and operations), `Gaia` Collaboration et al. (2018b): Summary of the contents and survey properties.

- Anders, F., Khalatyan, A., Chiappini, C., et al. 2019, *A&A*, 628, A94  
 Andrae, R., Fouesneau, M., Creevey, O., et al. 2018, *A&A*, 616, A8  
 Aschwanden, M. J. 2015, *ApJ*, 814, 19  
 Bailer-Jones, C. A. L., Andrae, R., Arcay, B., et al. 2013, *A&A*, 559, A74  
 Barentsen, G., Hedges, C., Saunders, N., et al. 2018, arXiv e-prints, arXiv:1810.12554  
 Barnes, S. A. 2003, *ApJ*, 586, 464  
 Bessell, M. S. & Brett, J. M. 1988, *Publications of the Astronomical Society of the Pacific*, 100, 1134  
 Bochanski, J. J., Hawley, S. L., Covey, K. R., et al. 2010, *AJ*, 139, 2679  
 Bochanski, J. J., West, A. A., Hawley, S. L., & Covey, K. R. 2007, *AJ*, 133, 531  
 Bokeh Development Team. 2019, `Bokeh`: Python library for interactive visualization  
 Boyajian, T. S., von Braun, K., van Belle, G., et al. 2013, *The Astrophysical Journal*, 771, 40  
 Burgasser, A. J., Cruz, K. L., Cushing, M., et al. 2010, *ApJ*, 710, 1142  
 Burgasser, A. J., Liu, M. C., Ireland, M. J., Cruz, K. L., & Dupuy, T. J. 2008, *ApJ*, 681, 579  
 Burgasser, A. J.,Looper, D. L., Kirkpatrick, J. D., & Liu, M. C. 2007, *ApJ*, 658, 557  
 Burgasser, A. J. & McElwain, M. W. 2006, *AJ*, 131, 1007  
 Burgasser, A. J., McElwain, M. W., Kirkpatrick, J. D., et al. 2004, *AJ*, 127, 2856  
 Candelaresi, S., Hillier, A., Maehara, H., Brandenburg, A., & Shibata, K. 2014, *ApJ*, 792, 67  
 Cantat-Gaudin, T., Jordi, C., Vallenari, A., et al. 2018, *A&A*, 618, A93  
 Carpenter, J. M. 2001, *The Astronomical Journal*, 121, 2851  
 Chambers, K. C., Magnier, E. A., Metcalfe, N., et al. 2016, ArXiv e-prints [arXiv:1612.05560]  
 Chang, S.-W., Byun, Y.-I., & Hartman, J. D. 2015, *ApJ*, 814, 35  
 Chang, S. W., Byun, Y. I., & Hartman, J. D. 2016, *VizieR Online Data Catalog*, J/ApJ/814/35  
 Clarke, R. W., Davenport, J. R. A., Covey, K. R., & Baranec, C. 2018, *ApJ*, 853, 59  
 Cruz, K. L., Burgasser, A. J., Reid, I. N., & Liebert, J. 2004, *ApJ*, 604, L61  
 Cruz, K. L., Reid, I. N., Liebert, J., Kirkpatrick, J. D., & Lowrance, P. J. 2003, *AJ*, 126, 2421  
 Curtis, J. L., Wolfgang, A., Wright, J. T., Brewer, J. M., & Johnson, J. A. 2013, *AJ*, 145, 134  
 Davenport, J. 2015, PhD thesis, University of Washington  
 Davenport, J. R. A. 2016, *ApJ*, 829, 23  
 Davenport, J. R. A., Becker, A. C., Kowalski, A. F., et al. 2012, *ApJ*, 748, 58  
 Davenport, J. R. A., Covey, K. R., Clarke, R. W., et al. 2019, *ApJ*, 871, 241  
 Davenport, J. R. A., Hawley, S. L., Hebb, L., et al. 2014, *ApJ*, 797, 122  
 Doi, M., Tanaka, M., Fukugita, M., et al. 2010, *AJ*, 139, 1628  
 Doorsselaere, T. V., Shariati, H., & Debosscher, J. 2017, *ApJS*, 232, 26  
 Douglas, S. T., Agüeros, M. A., Covey, K. R., et al. 2014, *ApJ*, 795, 161  
 Douglas, S. T., Agüeros, M. A., Covey, K. R., & Kraus, A. 2017, *ApJ*, 842, 83  
 Douglas, S. T., Curtis, J. L., Agüeros, M. A., et al. 2019, *ApJ*, 879, 100  
 Drake, J. J., Cohen, O., Yashiro, S., & Gopalswamy, N. 2013, *ApJ*, 764, 170  
 Eker, Z., Bakis, V., Bilir, S., et al. 2018, *MNRAS*, 479, 5491  
 Filippazzo, J. C., Rice, E. L., Faherty, J., et al. 2015, *ApJ*, 810, 158  
 Finkbeiner, D. P., Schlafly, E. F., Schlegel, D. J., et al. 2016, *ApJ*, 822, 66  
 Fischer, D. A. & Marcy, G. W. 1992, *ApJ*, 396, 178  
 Froning, C. S., Kowalski, A., France, K., et al. 2019, *ApJ*, 871, L26  
 Gaia Collaboration, Babusiaux, C., van Leeuwen, F., et al. 2018a, *A&A*, 616, A10  
 Gaia Collaboration, Brown, A. G. A., Vallenari, A., et al. 2018b, *A&A*, 616, A1  
 Gao, X. 2018, *ApJ*, 869, 9  
 Gizis, J. E. 2013, *ApJ*, 779, 172  
 Gizis, J. E. 2017, *ApJ*, 845, 33  
 Gonzalez, G. 2016, *MNRAS*, 459, 1060  
 Green, G. M., Schlafly, E. F., Finkbeiner, D., et al. 2018, *MNRAS*, 478, 651  
 Green, G. M., Schlafly, E. F., Zucker, C., Speagle, J. S., & Finkbeiner, D. P. 2019, arXiv e-prints, arXiv:1905.02734  
 Hawley, S. L., Davenport, J. R. A., Kowalski, A. F., et al. 2014, *ApJ*, 797, 121  
 Hawley, S. L. & Fisher, G. H. 1992, *ApJS*, 78, 565  
 Hilton, E. J. 2011, PhD thesis, University of Washington  
 Hilton, E. J., West, A. A., Hawley, S. L., & Kowalski, A. F. 2010, *AJ*, 140, 1402  
 Howard, W. S., Corbett, H., Law, N. M., et al. 2019a, *ApJ*, 881, 9  
 Howard, W. S., Corbett, H., Law, N. M., et al. 2019b, arXiv e-prints, arXiv:1907.10735  
 Howell, S. B., Sobeck, C., Haas, M., et al. 2014, *PASP*, 126, 398  
 Hunt-Walker, N. M., Hilton, E. J., Kowalski, A. F., Hawley, S. L., & Matthews, J. M. 2012, *PASP*, 124, 545  
 Ilin, E., Schmidt, S. J., Davenport, J. R. A., & Strassmeier, K. G. 2019, *A&A*, 622, A133  
 Jackman, J. A. G., Wheatley, P. J., Bayliss, D., et al. 2019, arXiv e-prints, arXiv:1902.00900  
 Karoff, C. 2016, *Nature Communications*, 7, 11058  
 Kerr, G. S. & Fletcher, L. 2014, *ApJ*, 783, 98

## References

- Aarnio, A. N., Matt, S. P., & Stassun, K. G. 2012, *ApJ*, 760, 9  
 Aarnio, A. N., Stassun, K. G., Hughes, W. J., & McGregor, S. L. 2011, *Sol. Phys.*, 268, 195  
 Aigrain, S., Parviainen, H., & Pope, B. J. S. 2016, *MNRAS*, 459, 2408  
 Alvarado-Gómez, J. D., Drake, J. J., Cohen, O., Moschou, S. P., & Garraffo, C. 2018, *ApJ*, 862, 93

- Kirkpatrick, J. D.,Looper, D. L.,Burgasser, A. J.,et al. 2010, ApJS, 190, 100  
 Kleint, L.,Heinzel, P.,Judge, P.,& Krucker, S. 2016, ApJ, 816, 88  
 Koch, D. G.,Borucki, W. J.,Basri, G.,et al. 2010, ApJ, 713, L79  
 Kowalski, A. F.,Hawley, S. L.,Wisniewski, J. P.,et al. 2013, ApJS, 207, 15  
 Kretzschmar, M. 2011, A&A, 530, A84  
 Lacy, C. H.,Moffett, T. J.,& Evans, D. S. 1976, ApJS, 30, 85  
 Lecavelier des Etangs, A.,Bourrier, V.,Wheatley, P. J.,et al. 2012, A&A, 543, L4  
 Lin, C. L.,Ip, W. H.,Hou, W. C.,Huang, L. C.,& Chang, H. Y. 2019, ApJ, 873, 97  
 Loyd, R. O. P.,France, K.,Youngblood, A.,et al. 2018, ApJ, 867, 71  
 Luger, R.,Kruse, E.,Foreman-Mackey, D.,Agol, E.,& Saunders, N. 2018, AJ, 156, 99  
 Lurie, J. C.,Davenport, J. R. A.,Hawley, S. L.,et al. 2015, ApJ, 800, 95  
 Maehara, H.,Shibayama, T.,Notsu, S.,et al. 2012, Nature, 485, 478  
 Mann, A. W.,Feiden, G. A.,Gaidos, E.,Boyajian, T.,& von Braun, K. 2015, ApJ, 804, 64  
 Mann, A. W.,Feiden, G. A.,Gaidos, E.,Boyajian, T.,& von Braun, K. 2016, The Astrophysical Journal, 819, 87  
 Maschberger, T.,& Kroupa, P. 2009, MNRAS, 395, 931  
 Mondrik, N.,Newton, E.,Charbonneau, D.,& Irwin, J. 2019, ApJ, 870, 10  
 Morin, J.,Donati, J. F.,Petit, P.,et al. 2008, MNRAS, 390, 567  
 Namekata, K.,Sakaue, T.,Watanabe, K.,et al. 2017, ApJ, 851, 91  
 Netopil, M.,Paunzen, E.,Heiter, U.,& Soubiran, C. 2016, A&A, 585, A150  
 Olivares, J.,Bouy, H.,Sarro, L. M.,et al. 2019, A&A, 625, A115  
 Olivares, J.,Sarro, L. M.,Moraux, E.,et al. 2018, A&A, 617, A15  
 Paudel, R. R.,Gizis, J. E.,Mullan, D. J.,et al. 2018, ApJ, 861, 76  
 Paudel, R. R.,Gizis, J. E.,Mullan, D. J.,et al. 2018, ApJ, 858, 55  
 Pecaut, M. J.,& Mamajek, E. E. 2013, ApJS, 208, 9  
 Priest, E.,& Forbes, T. 2002, A&A Rev., 10, 313  
 Queiroz, A. B. A.,Anders, F.,Santiago, B. X.,et al. 2018, MNRAS, 476, 2556  
 Raetz, S.,Stelzer, B.,Damasso, M.,& Scholz, A. 2020, arXiv e-prints, arXiv:2003.11937  
 Rayner, J. T.,Cushing, M. C.,& Vacca, W. D. 2009, ApJS, 185, 289  
 Rebull, L.,Stauffer, J.,Bouvier, J.,et al. 2016a, Astronomical Journal, 152, 113, bibtex: 2016AJ....152..113R bibtex[eid=113;adsurl=https://ui.adsabs.harvard.edu/abs/2016AJ....152..113R;adsnote=Provided by the SAO/NASA Astrophysics Data System]  
 Rebull, L. M.,Stauffer, J. R.,Bouvier, J.,et al. 2016b, AJ, 152, 113  
 Rebull, L. M.,Stauffer, J. R.,Hillenbrand, L. A.,et al. 2017, ApJ, 839, 92  
 Reid, I. N.,& Hawley, S. L. 2005, New Light on Dark Stars: Red Dwarfs, Low-Mass Stars, Brown Dwarfs, 2nd edn., Springer-Praxis books in astronomy and astrophysics (Berlin ; New York : Chichester, UK: Springer ; Praxis)  
 Reino, S.,de Bruijne, J.,Zari, E.,d'Antona, F.,& Ventura, P. 2018, MNRAS, 477, 3197  
 Sammis, I.,Tang, F.,& Zirin, H. 2000, ApJ, 540, 583  
 Schmidt, S. J. 2014, Mem. Soc. Astron. Italiana, 85, 741  
 Schmidt, S. J.,Hawley, S. L.,West, A. A.,et al. 2015, AJ, 149, 158  
 Schmidt, S. J.,Shappee, B. J.,Gagné, J.,et al. 2016, ApJ, 828, L22  
 Schmidt, S. J.,West, A. A.,Bochanski, J. J.,Hawley, S. L.,& Kielty, C. 2014, PASP, 126, 642  
 Schmidt, S. J.,West, A. A.,Hawley, S. L.,& Pineda, J. S. 2010, AJ, 139, 1808  
 See, V.,Jardine, M.,Vidotto, A. A.,et al. 2017, MNRAS, 466, 1542  
 Shakhovskaya, N. 1989, Sol. Phys., 121, 375  
 Shibayama, T.,Maehara, H.,Notsu, S.,et al. 2013, The Astrophysical Journal Supplement Series, 209, 5  
 Shibayama, T.,Maehara, H.,Notsu, S.,et al. 2013, ApJS, 209, 5  
 Skrutskie, M. F.,Cutri, R. M.,Stiening, R.,et al. 2006, AJ, 131, 1163  
 Tilley, M. A.,Segura, A.,Meadows, V.,Hawley, S.,& Davenport, J. 2019, Astrobiology, 19, 64  
 Toriumi, S.,Schrijver, C. J.,Harra, L. K.,Hudson, H.,& Nagashima, K. 2017, ApJ, 834, 56  
 Van Cleve, J. E.,Howell, S. B.,Smith, J. C.,et al. 2016, PASP, 128, 075002  
 Vanderburg, A.,& Johnson, J. A. 2014, Publications of the Astronomical Society of the Pacific, 126, 948  
 Vanderplas, J.,Connolly, A.,Ivezic, Z.,& Gray, A. 2012, in Conference on Intelligent Data Understanding (CIDU), 47 –54  
 Walkowicz, L. M.,Basri, G.,Batalha, N.,et al. 2011, AJ, 141, 50  
 Watanabe, K.,Shimizu, T.,Masuda, S.,Ichimoto, K.,& Ohno, M. 2013, ApJ, 776, 123  
 West, A. A.,Morgan, D. P.,Bochanski, J. J.,et al. 2011, AJ, 141, 97  
 West, A. A.,Weisenburger, K. L.,Irwin, J.,et al. 2015, ApJ, 812, 3  
 Wheatland, M. S. 2004, ApJ, 609, 1134  
 Wu, C.-J.,Ip, W.-H.,& Huang, L.-C. 2015, ApJ, 798, 92  
 Yang, H.,& Liu, J. 2019, ApJS, 241, 29  
 Yang, H.,Liu, J.,Gao, Q.,et al. 2017, ApJ, 849, 36  
 Yang, H.,Liu, J.,Qiao, E.,et al. 2018, ApJ, 859, 87  
 Yee, S. W.,Petigura, E. A.,& von Braun, K. 2017, ApJ, 836, 77

## Appendix A: Membership probabilities

To match catalogs on RA and declination we used the `astroML.crossmatch` tool for Python (Vanderplas et al. 2012). For the studies with classifiers we assigned membership probabilities as follows. In Gonzalez (2016):

$$\begin{aligned} p(M(\text{member})) &= 0.9, \\ p(BM(\text{binary member})) &= 0.9, \\ p(N(\text{non-member})) &= 0.1, \\ p(SN(\text{single non-member})) &= 0.1, \\ p(BN(\text{binary non-member})) &= 0.1, \\ p(U(\text{unknown member})) &= 0.5. \end{aligned}$$

In Curtis et al. (2013):

$$\begin{aligned} p(Y(\text{highest confidence member})) &= 0.9, \\ p(P(\text{possible/probable member})) &= 0.7, \\ p(N(\text{not likely/non-member})) &= 0.7, \\ p(B(\text{photometry consistent with blue stragglers})) &= 0.0. \end{aligned}$$

In Rebull et al. (2017):

$$\begin{aligned} p((\text{best})) &= 0.9, \\ p((\text{ok})) &= 0.6, \\ p((\text{else})) &= 0.1. \end{aligned}$$

Members from Rebull et al. (2016a); Douglas et al. (2017); and Gaia Collaboration et al. (2018a) were assigned  $p = 0.9$  if they appeared in the final catalog.

Table A.1 gives an overview over different membership catalogs. Figure A.1 shows membership probability histograms of the final sample broken down by membership source.

## Appendix B: Cluster parameters

We compiled various age, distance, and metallicity values from the literature for the clusters in this study. Table B.1 shows that most studies independently arrived at similar results for all our clusters. The adopted parameters are emphasized, and were chosen based on consistency with prior work, uncertainties provided with the results and the data used for the study (newer catalogs were preferred).

## Appendix C: Broadband photometry: quality cuts and conversions

We required  $\text{flux}/\text{flux\_error} \geq 10$  for Gaia G, BP, and RP bands. We require that the 2MASS measurements for  $J$ ,  $H$ , and  $K$  to be "A". "A" meant that measurements had  $S/N > 10$  and  $\sigma < 0.11$ . For PanSTARRS photometry, we required that the QF\_OBJ\_GOOD quality filter flag was set. SDSS and PS1  $ugriz$  bands were similar but not identical, but could be converted using Table 2 in Finkbeiner et al. (2016).

## Appendix D: Modified Maximum Likelihood Estimator

As a means to arrive at results efficiently, and as consistency check to the method derived from Wheatland (2004) we fitted  $\alpha$  to the FFDs in  $ED$  and  $E_{Kp}$  space using a Modified Maximum

Likelihood Estimator (MMLE, Maschberger & Kroupa 2009). The logarithm of the likelihood function  $\mathcal{L}$  that had to be maximized was given by the authors in Eq. (8) in their manuscript:

$$\log \mathcal{L} = n \log(1 - \hat{\alpha}) - n \log(x_{\max}^{1-\hat{\alpha}} - x_{\min}^{1-\hat{\alpha}}) - \hat{\alpha} \sum_{i=1}^n \log x_i \quad (\text{D.1})$$

where  $x_i$ ,  $x_{\max}$ , and  $x_{\min}$  were the detected flare energies, and the upper and lower limits for detection, respectively.  $n$  was the total number of flares. The estimate for  $\alpha$  would be biased in practice because the value used for  $x_{\max}$  would be the maximum energy that was measured, and not the underlying upper limit. The stabilization transformation suggested by the authors (Eq. (12) in Maschberger & Kroupa 2009) was then applied to the solution for  $\alpha$  to account for this bias:

$$\alpha = 1 + \frac{n}{n-2}(\hat{\alpha} - 1) \quad (\text{D.2})$$

Using the MMLE method on the full sample of flares in  $E_{Kp}$  and  $ED$  space we obtained  $\alpha_{\text{erg}} = 1.85$  and  $\alpha_s = 1.95$ , respectively, indicating a marginally flatter power law than the predictive model ( $\alpha_{\text{erg}} = 1.87$ ,  $\alpha_s = 1.99$ ).

## Appendix E: Rotation and flaring

More energetic flares can be expected from faster rotating stars (Candelaresi et al. 2014; Doorsselaere et al. 2017; Yang et al. 2017). Findings that flares with intermediate Rossby number appear to flare more than fast and slow rotators (Mondrik et al. 2019) **could not be reproduced here** or in the EvryFlare survey (Howard et al. 2019b). If enhanced flaring can be interpreted as an increase in the stellar angular momentum loss rate flaring activity can be used to inform the cause of variation in the spin-down efficiency. An example of such variations is the apparent temporary stalling of spin-down seen in K dwarfs in NGC 6811 (Curtis+2019). The authors favored a scenario in which the stellar core transfers momentum onto the envelope but did not rule out the possibility of a decreased magnetic braking efficiency. In the latter scenario, these stars should flare less. We used rotation periods derived from K2 light curves for the Pleiades (Rebull et al. 2016b), the Hyades and Praesepe (Douglas et al. 2019), to **illuminate the rotation-flaring relation** at fixed ages. The distribution of rotation periods in the temperature bins is shown in Fig. E.1.

## Appendix F: Universality of power law exponent $\alpha$

We searched the literature for studies work where power laws were fitted to FFDs of flares in the optical regime using different methods. Fig. F.1 lists the overview. While particular studies consistently find values somewhat above or below  $\alpha \approx 2$ , the comparison of different studies points towards unresolved systematic errors in all these studies.

**Table A.1.** Membership catalogs overview. No distance are given for Hyades we adopted individual distances for all members.

source	type	clusters covered	notes
Curtis et al. (2013)	classifier	Rup 147	
Douglas et al. (2014)	probability	Hyades, Praesepe	meta study
Gonzalez (2016)	classifier	M67	
Rebull et al. (2016a)	members list	Pleiades	meta study
Rebull et al. (2017)	classifier	Praesepe	meta study
Douglas et al. (2017)	members list	Praesepe	meta study
Gaia Collaboration et al. (2018a)	members list	Hyades, Rup 147, Pleiades, Praesepe	Gaia DR2, (1)
Cantat-Gaudin et al. (2018)	probability	Rup 147, Pleiades, Praesepe	Gaia DR2
Gao (2018)	probability	M67	Gaia DR2
Reino et al. (2018)	probability	Hyades	Gaia DR1, (1)
Olivares et al. (2018)	probability	Pleiades	Gaia DR2, DANCe
Olivares et al. (2019)	probability	Rup 147	Gaia DR2, DANCe

**Notes.** DANCe: DANCe membership study project. (1) Positions for Hyades were propagated to epoch 2000 using Gaia proper motions.

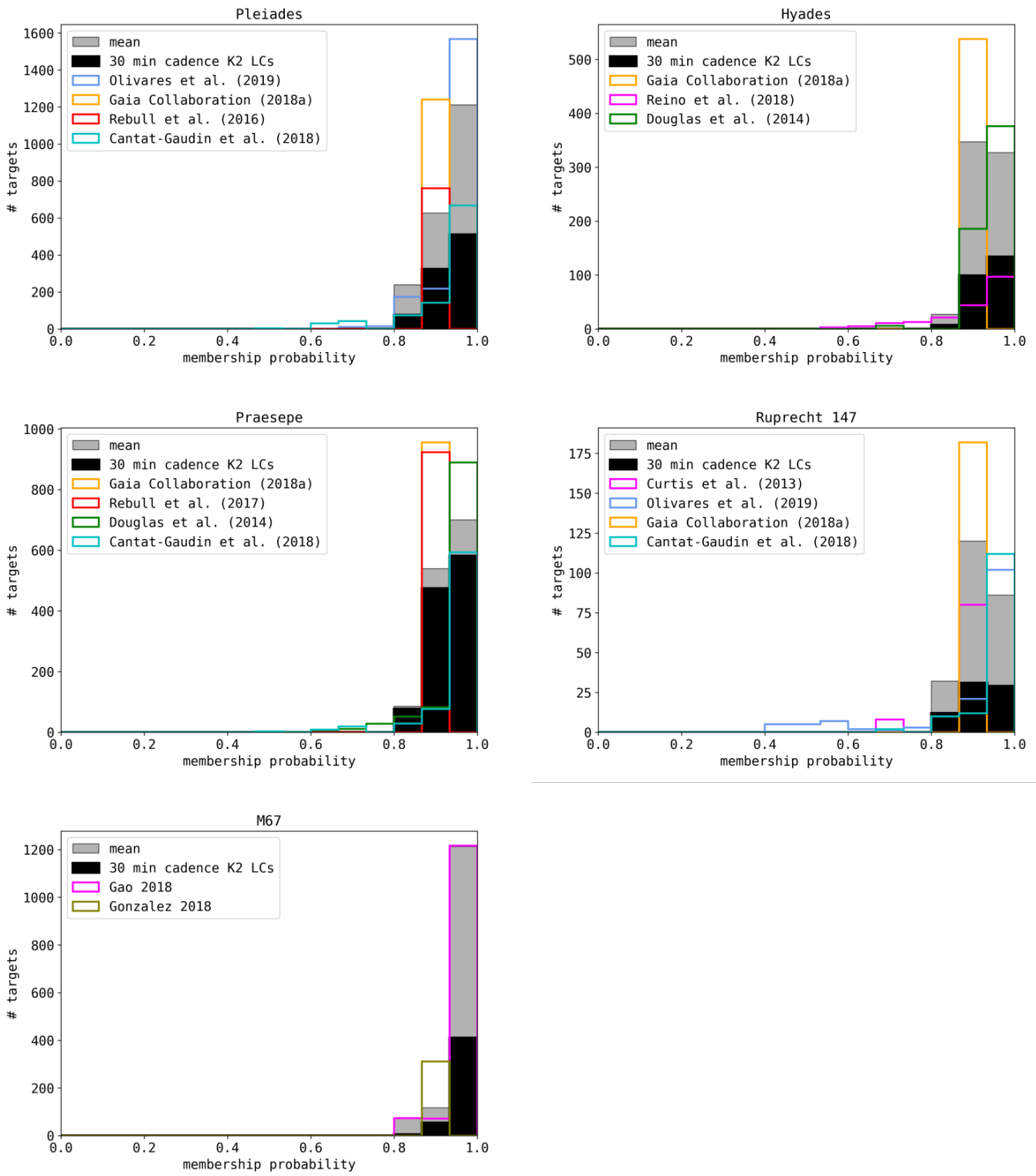


**Fig. A.1.** OC membership histograms and selected targets.

**Table B.1.** Non-exhaustive literature overview over OC parameters.

cluster	source	distance [pc]	age [Myr]	[Fe/H]
<b>Pleiades</b>	<b>adopted in this work:</b>	135.6	$135 \pm 25$	$-0.037 \pm 0.026$
Pleiades	Bossini et al. (2019) <sup>a</sup>		$86.5 \pm 6$	
Pleiades	Cantat-Gaudin et al. (2018)	135.6		
Pleiades	Gossage et al. (2018)		$135 \pm 25$	
Pleiades	Yen et al. (2018)	126.3	$141.3 \pm 170$	
Pleiades	Chelli and Duvert (2016)	139		
Pleiades	Netopil et al. (2016)			-0.01
Pleiades	Dahm (2015)		$112 \pm 5$	
Pleiades	Scholz et al. (2015)	130	120	
Pleiades	Conrad et al. (2014)			$-0.037 \pm 0.026$
Pleiades	Melis et al. (2014)	136		
Pleiades	Bell et al. (2012)	135	125	
<b>Hyades</b>	<b>adopted in this work:</b> <sup>c</sup>		$690 \pm 160$	$0.13 \pm 0.02$
Hyades	Gaia Collaboration (2018)		$690 \pm 160$	
Hyades	Gossage et al. (2018)		680	
Hyades	Liu et al. (2016)			$\pm 0.02$
Hyades	Netopil et al. (2016)			0.13
Hyades	Taylor and Joner (2005)			$0.103 \pm 0.008$
Hyades	Cummings et al. (2005)			$0.146 \pm 0.004$
Hyades	Salaris et al. (2004)		650	0.15
Hyades	Perryman et al. (1998)		$625 \pm 50$	
Hyades	Martin et al. (1998)		$650 \pm 70$	
<b>Praesepe</b>	<b>adopted in this work:</b>	185.5	$750 \pm 3$	0.16
Praesepe	Bossini et al. (2019)		$750 \pm 3$	
Praesepe	Cantat-Gaudin et al. (2018)	185.5		
Praesepe	Gossage et al. (2018)		590	
Praesepe	Yen et al. (2018)	183	$794 \pm 253$	
Praesepe	Netopil et al. (2016)			0.16
Praesepe	Scholz et al. (2015)	187	832	
Praesepe	Boesgaard et al. (2013)			0.12
Praesepe	Boudreault et al. (2012)	160	630	
Praesepe	Salaris et al. (2004)	175	650	
<b>Rup 147</b>	<b>adopted in this work:</b>	305	$2650 \pm 380$	$0.08 \pm 0.07$
Rup 147	Bragaglia et al. (2018)			$0.08 \pm 0.07$
Rup 147	Cantat-Gaudin et al. (2018)	305		
Rup 147	Gaia Collaboration (2018)	309	$1995 \pm 404$	
Rup 147	Torres et al. (2018)	283	$2650 \pm 380$	
Rup 147	Curtis (2016) <sup>b</sup>			$0.10 \pm 0.02$
Rup 147	Scholz et al. (2015)	270	1953	
Rup 147	Curtis et al. (2013)	300	$3125 \pm 125$	$0.07 \pm 0.03$
<b>M67</b>	<b>adopted in this work:</b>	908	$3639 \pm 17$	$-0.102 \pm .081$
M67	Bossini et al. (2019)		$3639 \pm 17$	
M67	Netopil et al. (2016)			0.03
M67	Scholz et al. (2015)		$3428 \pm 147$	
M67	Conrad et al. (2014)			$-0.102 \pm .081$
M67	Dias et al. (2012)	908	4300	
M67	Oïehag et al. (2011)	880	4200	0.02

**Notes.** <sup>(a)</sup> Bossini et al. (2019) noted some caveats for their determination of ages of young clusters, for which they used Gaia DR2 photometry for isochrone fitting. <sup>(b)</sup> Curtis (2016) reanalysed HIRES spectra using an improved spectroscopic method as compared to Curtis et al. (2013). <sup>(c)</sup> We did not adopt a mean value for the Hyades distance because the cluster members are on average closer than 50 pc.

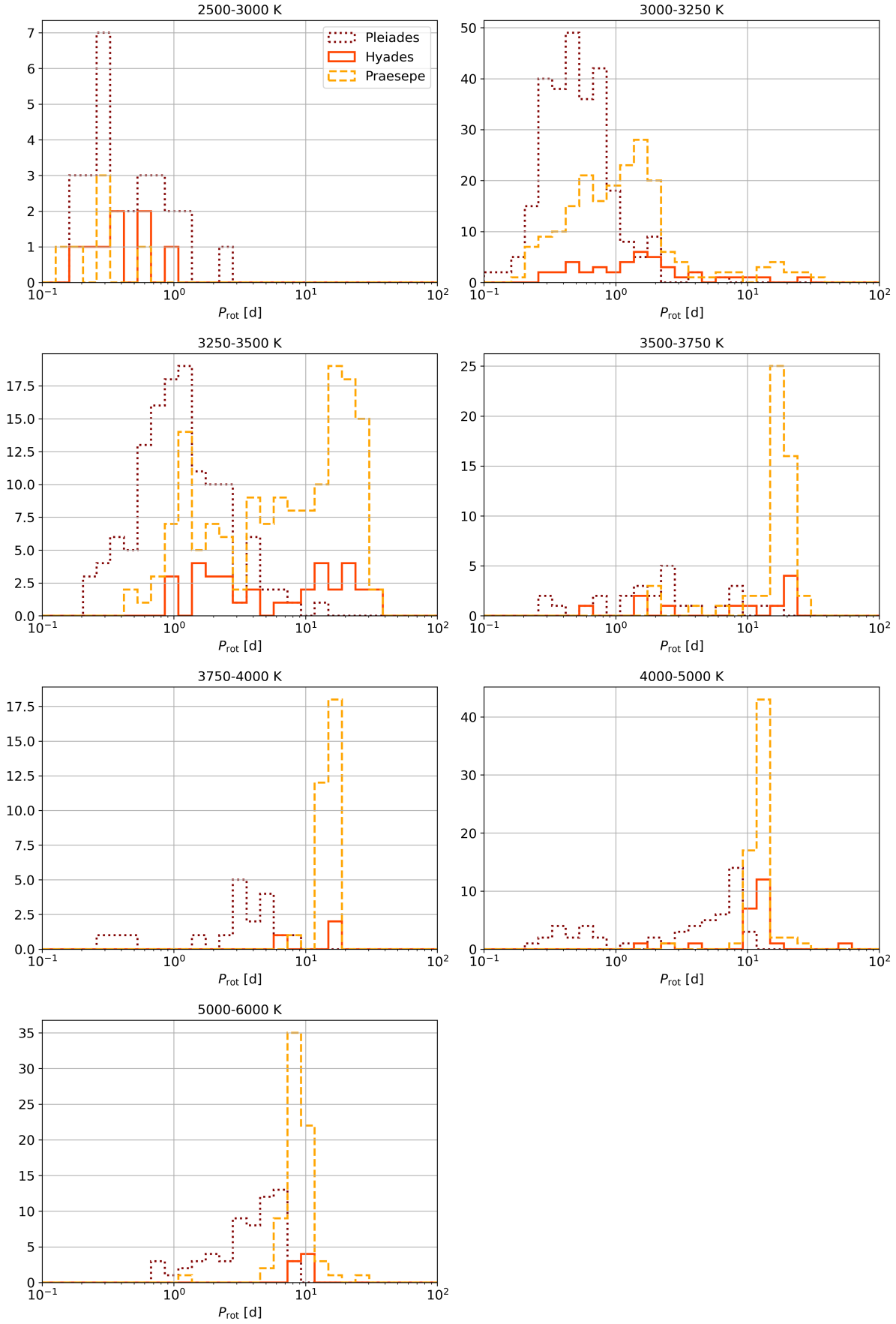


**Fig. E.1.** Rotation histograms for the cluster members that were searched for flares and had measured rotation periods  $P_{\text{rot}}$ . Rotation periods were taken from Douglas et al. (2019) for the Hyades and Praesepe, and from Rebull et al. (2016b) for the Pleiades.

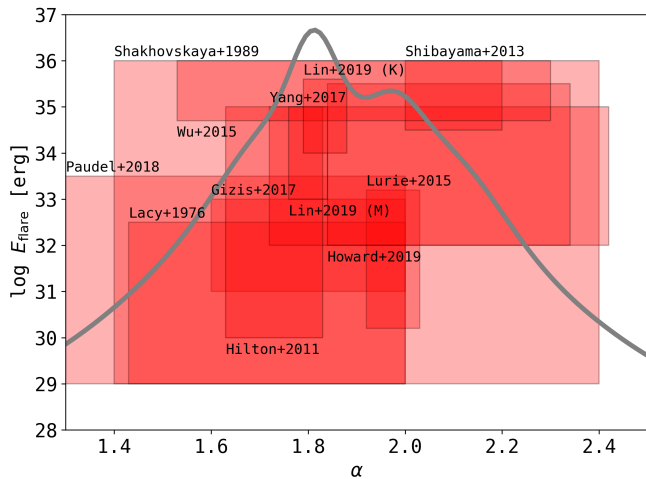


**Fig. F.1.** Literature overview over power law fits to FFDs. Red triangle indicate the energy range in which flares were detected, and the range of values determined for the power law exponent including quoted uncertainties and combining multiple FFDs if any. Lacy et al. (1976) pioneered in statistical flare studies using observations of eight UC Ceti stars. Shakhovskaya (1989) analyzed monitoring data from several dozen active early K to late M dwarfs. Hawley et al. (2014) used flares from M dwarfs in the original Kepler observations for their FFDs. A number of studies focused on solar-type and G dwarfs stars in Kepler (Maehara et al. 2012; Wu et al. 2015; Shibayama et al. 2013). Hilton (2011) derived  $\alpha$  from ground-based observations of M dwarfs. Lurie et al. (2015) were based on Kepler short cadence light curves of two active M5 dwarfs in Kepler. Davenport (2016) searched the entire Kepler catalog for flares on lowGizis (2017) constructed an FFD for 22 flares on an M7 dwarf. Yang et al. (2017) followed up on Davenport (2016) in searching the entire Kepler catalog for flares. Paudel et al. (2018) studied M6-L0 dwarfs in K2 short cadence data. Howard et al. (2019a) found over 500 superflares on 284 stars in the course of the Evryscope all-sky survey. Lin et al. (2019) (M) and (K) were based on M and K dwarf flares in K2 long cadence light curves.